ABSTRACT

Title of dissertation: HIGHLY EFFICIENT, MEGAWATT CLASS RF POWER SOURCES FOR MOBILE IONOSPHERIC HEATERS

Jayakrishnan Appanam Karakkad, Doctor of Philosophy, 2020

Dissertation directed by: Prof. Thomas M. Antonsen Jr., Electrical and Computer Engineering

In this thesis, we consider the development of a highly efficient, grid-less tetrode as a megawatt-level RF source in the 3 to 10 MHz range for application in a mobile ionospheric heater. Such a heater has potential advantages over the stationary facilities, such as HAARP (High-Frequency Active Auroral Research Program), found at high latitude. The considered device operates in class D mode with an annular electron beam allowing realization of high efficiency. The beam current is controlled using an annular modulating electrode (mod-anode) placed around the annular emitter on the cathode. This feature removes the traditional semi-transparent grid and the problems associated with interception of current beam at the grid.

Three different device configurations based on differing magnetic field confinement were considered. Model A, which has a constant focusing magnetic field and no beam compression, offers the highest interaction efficiency. However, to generate a uniform and constant magnetic field over the whole device length would require the use of a large and bulky

solenoid. This makes the setup in the case of Model A much larger (and much heavier). Model B has a magnetic field that is up-tapered from the cathode towards the anode and collector where the bulk part of the solenoid is located. This configuration retains the compression of the electron beam to maintain a high efficiency while keeping the size of the device manageable. It has a lower efficiency than Model A, but it provides a larger cathode area in than in Model A which mitigates cathode loading. In the case of Model C, there no guiding magnetic field and is the most compact, but its interaction efficiency is the lowest among the three device types. Model C also uses two modulating anodes maintained at varying voltages to provide electrostatic focusing of the electron beam. It is still operated in the class D regime by switching the two mod-anodes of Model C on and off together. However, the voltage swing will be much larger compared to Model A.

A theoretical analysis to find the optimal operating point for model A is presented. In particular, the trade-off between the peak current and the duration of the current pulse is analyzed. The beam distributions in axial and transverse momenta and in total electron energies, before and after the decelerating gap, calculated using the Michelle code are presented for Model A.

Using static-case Michelle simulation results, the instantaneous and average device efficiencies of the three models were maximized while reducing the device size by studying the influence of electrode geometry (Anode-Cathode Gap, and Anode-Collector gap and shapes) on the device efficiency. After optimizing the device geometry for these three different models, time-domain simulations with secondary electrons were performed. For model A, it is found that during the portion of the RF cycle when the beam current is on, secondaries emitted from the collector are driven back into the collector by the incoming primary beam. When the beam is

switched off, secondaries can stream back into the tetrode and have a small negative impact on efficiency. We present a design in which the secondary electrons are eventually absorbed at the collector, rather than at the cathode or anode. For model B, most of the secondary electrons are trapped in the collecting region due to an effect called magnetic mirroring from the up tapering of the magnetic field towards the collector region. In Model C, the secondary electrons are largely scattered throughout the tetrode due to the lack of magnetic field confinement making it much harder to prevent the loss of efficiency.

In short, three different versions of the grid-less tetrode have been proposed and studied. The optimized version of these devices have efficiencies ranging from 81% to 91.5%. The choice of the optimal design for real systems may depend on a number of tradeoffs. In the situations where the weight and size of a system play a crucial role, Model C could be more preferable with the penalty of lower efficiency. In turn, Model A can offer the highest efficiency, but the solenoids required for maintaining a constant magnetic field along the entire device could be very heavy and bulky. In comparison, Model B offers a middle ground among the three models on compactness and efficiency.

HIGHLY EFFICIENT, MEGAWATT CLASS RF POWER SOURCES FOR MOBILE IONOSPHERIC HEATERS

by

Jayakrishnan Appanam Karakkad

Dissertation submitted to the Faculty of the Graduate school of the
University of Maryland, College Park, in partial fulfillment
of the requirements for the degree of
Doctor of Philosophy
2020

Advisory Committee:
Professor Thomas M Antonsen Jr., Chair/Advisor
Professor Edward Ott
Professor Thomas E. Murphy
Professor Adil B. Hassam
Dr. Gregory S. Nusinovich
Dr. Antonio C. Ting
Dr. Brian L. Beaudoin

Dedication

I would like to dedicate this to my parents, Subramanian Appanam Karakkad and Geetha Namboodiri, my brother and his wife, Sujith Appanam Karakkad, and Rachana Satheeshkumar. Your unconditional love and support have made this work achievable.

Acknowledgements

My Ph.D. thesis work would not be successful without the contributions of many people. I would like to thank them here. Words are certainly not enough to express my deep gratitude to them all.

First of all, I would like to thank Professor Thomas Antonsen for his valuable guidance during my tenure as a graduate student. Without his endless patience, guidance, and encouragement, this thesis would have not been possible. I would also like to thank Dr. Gregory Nusinovich for his valued guidance in both the theoretical and simulation part of this thesis. He has been a great pillar of guidance and encouragement from time to time both formally and informally. I would like to thank Dr. Antonio Ting for all his valuable advice and help with polishing this thesis. I would like to express my gratitude to Brian Beaudoin, for his helpful advice and guidance with the Michelle PIC code.

I am also grateful to Professor Edward Ott, Professor Thomas Murphy, and Professor Adil Hassam for serving on the advisory committee.

Contents

List of Tables

Number **Page**

List of Figures

Number **Page**

Chapter 1: Mobile Ionospheric Heaters and their RF power source

1.1 Motivation

Ionospheric modification refers to the induced changes in the ambient properties of the ionosphere (ionized part of earth's upper atmosphere). While it is true that naturally occurring events can have long lasting and deep effects on the ionosphere, we are interested in studying those effects that can be controlled and repeated to our needs. This active Ionosphere Modification (IM) allows users to develop new applications based on possibilities to control and exploit triggered ionospheric and magnetospheric processes. The key method in triggering these processes is ionospheric heating. Heating the ionosphere with Radio Frequency (RF) waves is of interest for a variety of scientific and practical reasons (see, e.g., Ref. [1] [2]). The RF frequency needed for effective heating (3-10 MHz) corresponds to wavelengths of 30-100 m.

So far a majority of the studies involve the use of ground-based heaters [3]. It should however be noted that for many applications a mobile ionospheric heater is much more attractive. Past IM experiments conducted at high latitudes have indicated strong dependence of ionospheric processes on geomagnetic latitude. Thus, mobile ionospheric heaters will be able to provide us with quantitative results in regarding the relation between IM and geomagnetic latitudes without expensive ground-based installations.

In 2012 the Air Force Office of Scientific Research (AFOSR) started a new program aimed at studying the possibility to develop transportable ionospheric heating facilities capable of more efficient ionospheric modifications than existing stationary facilities located, as a rule, at high latitudes.

Existing facilities such as High frequency Active Auroral Research Program (HAARP) [3] employ large antenna arrays (300-400 m) achieving sufficient antenna gain to operate with total power of the order of several megawatts. HAARP has 180 transmitters of maximum 20 kW each. It is desired to have a transportable heating facility with a much smaller antenna array (30-60 m). To achieve the same radiated power density it is necessary to develop highly efficient, relatively compact RF sources capable of operation in a 3-10 MHz frequency range at about 1 MW power level, we will then require an array of 16 such individual units operating at a total of 16 MW. At present, there are no available RF tubes with such parameters: the tubes used at HAARP are gridded triodes of much lower power level. These devices cannot be scaled to the required power levels because of the restrictions imposed by the thermal management of their grids that intercept some of the beam electrons.

1.2 RF power source

In the frequency range of interest, 3-10 MHz, a promising source, which is capable of both high power and high efficiency, is a grid-less version of the tetrode. The principle behind signal amplification of our grid-less tetrode can be understood by studying similar kind of devices such as the klystron and klystrode [4-6].

A klystron is a linear beam vacuum tube invented in 1937. It consists of an electron gun that injects a linearly propagating electron beam through a circuit consisting of two resonant cavities separated by a drift tube. The beam is maintained at the anode potential. The first resonant cavity is excited by an input microwave signal. The electron beam then passes through a short gap in the input cavity where the cavity field modulates the beam velocity. The transit time

(time taken for the electrons to traverse the interaction space) is quite small compared with the period of the input signal, and the velocity modulation of an electron depends on the orientation and magnitude of the microwave field in the interaction space. The drift-tube is field free, the faster electrons overtake the slower electrons, and this leads to formation of electron bunches. Once these electron bunches passes through the interaction space of the second cavity, it excites microwaves from which it is possible to extract a microwave signal stronger than the input signal.

The klystrode or an Inductive Outpute Tube (IOT) is a specialized linear beam vacuum tube. The klystrode is a cross between a klystron and a triode. It has a control grid in front like a triode and klystron like gun and output cavity. It is a density modulated device where the RF voltage on the control grid modulates the current passing through the grid. In a klystrode the time dependence of the beam current is controlled by the voltage on a grid. It is thus possible to form bunches in the gun region with different temporal waveforms and thus operate in different regimes. In Class A operation, the beam current is modulated in time. However, the modulation is not total, and some current is always flowing. The current that is flowing during the accelerating phase of the cavity electric field reduces the amount of power extracted from the beam and degrades efficiency. In Class B and C operation the beam current is turned off for portions of a cycle, and is on to some degree for the remaining portion: on for 180 degrees in Class B and <180 degrees in Class C respectively. Finally, there is Class D operation in which the beam current is either totally on or off, and the level of the signal is encoded in the fraction of the time the beam current is on. In this mode of operation the beam current can be on only for short as ~90 degrees when the decelerating electric field is maximum, resulting in maximum power extracted from the beam.

Beam modulation without a grid is important because electron beam interception by grid elements is one of the most severe factors limiting klystrode power in high average power regimes. In this novel grid-less device, whose basic operation is discussed in section **1.2.1**, an electron beam is accelerated from a cathode and fully modulated by an electrode near the cathode. This produces a pulsating current that excites a resonant circuit.

Parameters	**250 kW CW IOT(Los Alamos) [6]**	**10TD2130 (E2V) [7]**	**VKP-9050 IOT Amplifier (CPI)**	**VKP-9130 IOT Amplifier (CPI)**	**100 kW CW Multibeam IOT [8]**
Frequency (MHz)	267	470-810	500	1300	1300
Output power (kW)	250 CW	80-60 CW	90 CW	30 CW or 90 pulsed	100 CW
Beam voltage (kV)	65	36-38	40	35/42	24
Beam current (A)	5.5	2.2-1.57	3.5	1.3/3.4	4
Efficiency (%)	>70	65-58	>65%	>60%	≅80
Operating regime	Class B	Class B	Class B	Class B	Class C

Table 1. A table summarizing the current state of the art along with proper referencing of their sources

To date, a number of klystrodes operating at higher frequencies have been developed. Table 1 summarizes the state-of-the-art in this development [7-9]. Also, the U.S Naval Research

Laboratory investigated via numerical simulation the dynamics of an IOT with the aim of improving output power [10], and a 350 MHz multiple beam IOT capable of generating 200 kW with about 70 % efficiency and 22 dB predicted gain was proposed in [11].

As indicated in Table 1, IOTs typically operate in the frequency range of 200 MHz-1300 MHz. These devices all operate in class B and C mode and offer efficiencies ranging from 60-80%. The device we consider operates at much lower frequency, 3-10 MHz, which has two important consequences. First, the beam can be fully modulated by a solid-state driver allowing for class D operation. Second, the electron transit time through the device is much shorter than the wave period, and as a consequence, the time evolution of the device can be analyzed as a sequence of self-consistent equilibria.

High efficiency operation can be achieved by operating in class D mode, in which the electron beam is pulsed with a period corresponding to that of the RF and with a duty factor that is sufficiently small to allow all electrons to see nearly the same decelerating field. If this is the case, selecting the duty factor thus involves a trade-off between minimizing the temporal variation of the decelerating field while the beam is on and minimizing the effects of space charge in the intense beam.

1.2.1 Device basics

The schematic arrangement of the basic device and its circuitry are shown in Fig. 1. We note that in these initial studies a flat collector is modeled. This will be replaced by more useful and complicated geometries when we study the collector surfaces in detail.

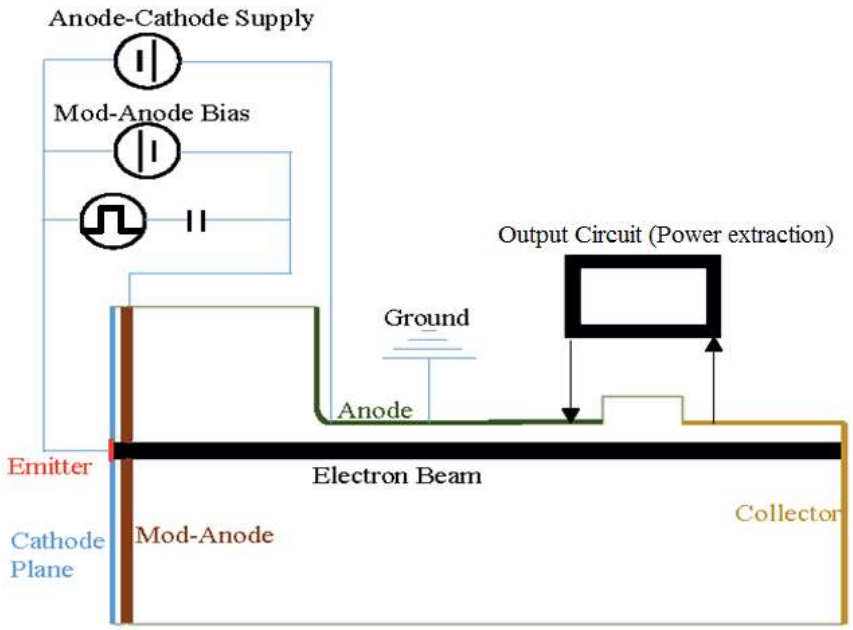

Fig. 1. Schematic arrangement of the device and its circuitry

The device has several features aimed at maximizing efficiency. Electrons are emitted from a cathode held at a potential $-V_{AK}$ and accelerated towards a grounded anode. The beam is gated by a modulation anode that can turn the cathode emission on and off without intercepting any beam current. This feature eliminates the conventional semi-transparent grid and the problems associated with beam current intercepted by the grid. The beam is annular for reduced space charge beam effects thus ensuring that the electrons passing through the device experience nearly the same accelerating and decelerating fields. Electrons pass a decelerating gap across which the RF field appears, and are collected by a collection surface. The collected current returns to ground through an energy extraction circuit which generates the RF field in the decelerating gap. The electron beam must propagate from the cathode to the collector with minimal spreading to insure that all electrons are collected at the lowest possible potential. The operating parameters of the device are chosen to be 70 kV of anode to cathode voltage and a

beam current of 70 A, under the considerations of available MW level of beam power for RF generation and sustainable current loading factor for the cathode.

A sample output circuit for this device is shown in Fig. 2. It is a pi-type circuit with reactive elements, driven by a current source representing the beam, and feeding a resistive load representing a transmission line or tuned antenna [15]. The pi-circuit is highly resonant and presents the input impedance needed to decelerate a 70 kV, 30 A beam with a rectangular temporal current profile. The main components of the pi-circuit are the input capacitor C_1, the output capacitor C_2, and the inductor L_{12} connecting the two capacitors. The circuit feeds an output impedance, R_o. The circuit parameters are selected so that the circuit presents a real impedance to the current source I_{Beam} at the operating frequency. The broad frequency range requires the circuit to be tunable, and the need for a constant decelerating voltage requires constant impedance, the study for engineering such a constant impedance pi circuit will be discussed in future publication. We note that because the circuit is highly resonant the voltage that develops across decelerating gap will always vary sinusoidally in time. That is, it will have a low harmonic content. Similarly the voltage delivered to the load will also be free of harmonics.

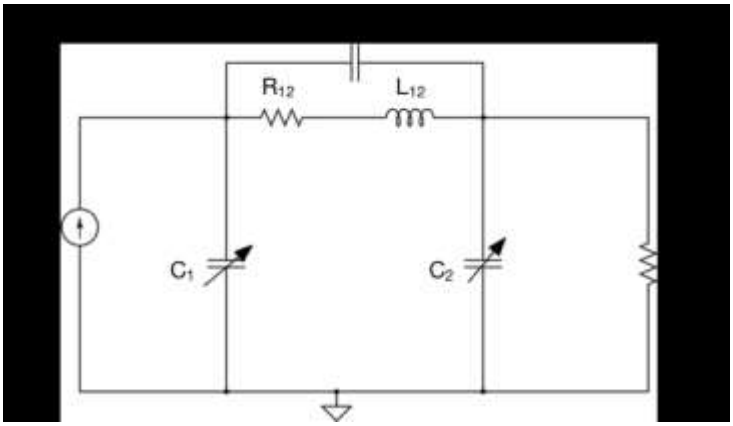

Fig. 2. Pi-circuit model with parasitic elements for L12 (C12 and R12) included

1.3 Calculation of device efficiency

In general, the energy extracted from the electrons and the efficiency can be estimated as follows. It is important to note that the transit time of electrons through the device (moreover, through the decelerating gap) is much shorter than the RF period. For example, when the voltage is in the range of 30-70 kV, the time for an electron to travel from the emitter to collector (T_{tr}) is on the order of 1 ns, while the 3-10 MHz frequency corresponds to a 100-300 ns RF period. Since

$$T_{tr} \cong \frac{L}{V_Z} \ll \frac{1}{\omega} \tag{1}$$

The RF field can be considered to be steady during the transit of individual electrons. However, electrons entering the device at different times during the pulse will experience different phases of the RF field and produce different efficiencies. Electrons emitted from the cathode at potential $-V_{AK}$ are accelerated to a potential close to the anode and are then decelerated and collected at a potential $-V_{RF}(t)$.

During this process the electrons have been given an energy eV_{AK} by the power supply and have given an energy eV_{RF} to the oscillating RF field on their return through the extraction circuit. Thus, for each electron the efficiency of energy conversion is

$$\eta_I(t) = \frac{V_{RF}(t)}{V_{AK}} \tag{2}$$

We refer to this as the instantaneous efficiency. Since the RF field varies in time as $V_{RF}(t) = V_{RF,\max} \sin \omega t$, the average device efficiency is determined by averaging over the phases

of the RF field during which the beam is on. For a flat top beam current micro-pulse of duration T centered in time on the peak of the RF field the average efficiency is given by

$$\bar{\eta} = \eta_{I,\max}\eta_{\varphi} \tag{3}$$

Where $\eta_{I,\max} = V_{RF,\max} / V_{AK}$ is the peak instantaneous efficiency and

$$\eta_{\varphi} = \frac{\sin(\theta)}{(\theta)} \tag{4}$$

represents the efficiency reduction due to time averaging. In Eq. (4) we introduced θ describing the pulse duration: $2\theta = \omega T$ is the duration of the beam micro-pulse in radians.

The average efficiency given in Eq. (3) is the product of two factors. Maximizing efficiency requires making each of these factors as large as possible. The maximum value of the RF voltage $V_{RF,\max}$ in Eq. (2) is limited by a combination of space charge effects and transverse acceleration. In particular, as a result the maximum RF field is limited to a value less than the V_{AK}. Exceeding this limiting value causes reflection of the slowest electrons back to the cathode. This maximum value of the RF voltage depends on the beam current, the proximity of a thin annular electron beam to the metallic walls, and on the value of the focusing magnetic field suppressing electron transverse acceleration. In the case of the efficiency reduction given in Eq. (4), maximizing this factor means making the micro-pulse duration T as small as possible. If the peak current is fixed, shortening the pulse duration leads to a reduction in average beam power. Thus, it is desired to operate with the highest peak current possible. An increase in peak current, however, reduces the instantaneous efficiency and makes the evaluation of both factors in Eq. (3) necessary to obtain an optimum operating point.

Three different configurations have been investigated and are shown in Fig. 3: Model A, which has a uniform magnetic field (0.1T) and no beam compression; Model B, which has a tapered guiding magnetic field (peak field of 0.1T) and thus provides beam compression, and Model C, which has no guiding magnetic field. Model A has the simplest configuration, thus allowing us to perform analysis of various factors such as maximum achievable efficiency and maximum limiting current. Model B is the more practical case with a guiding magnetic field that compresses the beam for better beam performance and power extraction efficiency. Finally Model C is an idealized device model that doesn't require bulky solenoid setup while still remaining compact. It offers many practical advantages from the simple magnet-free configuration at the expense of some loss in the power extraction efficiency.

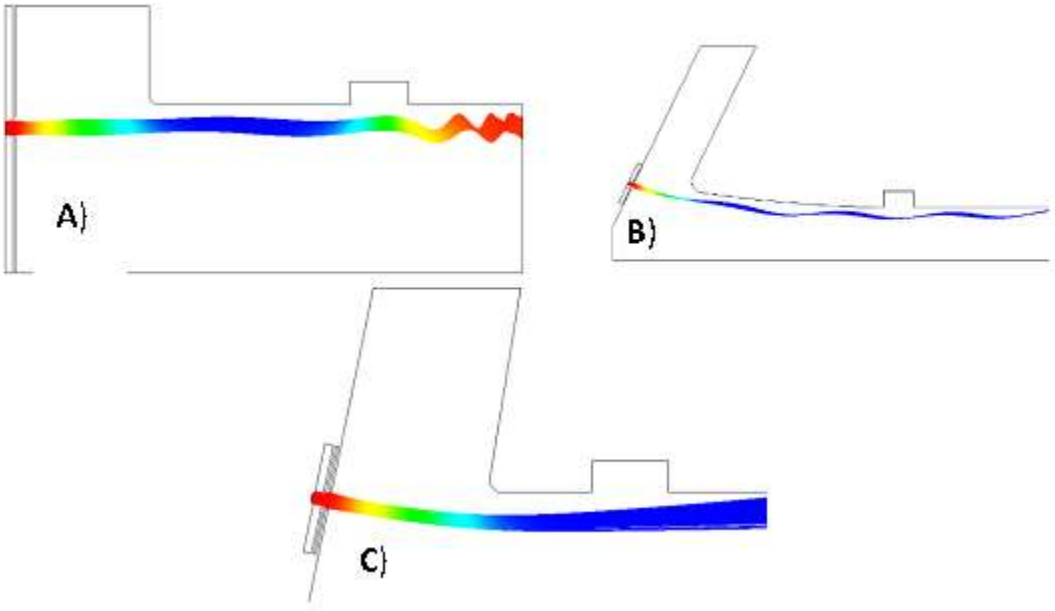

Fig. 3. Three models simulated in Michelle code

A detailed analysis of beam transport and efficiency for Model A, B and C are presented in chapters 2, 3 and 4 respectively. All simulations are done by using the particle-in-cell (PIC) code Michelle [16-17]. The Michelle code is capable of simulating the generation of secondary

electrons and its interaction with the primary electrons. The addition of secondary electrons generally has a negative impact on the device efficiency. The secondary electrons behave differently in each of these models. Unlike Model A where most of the secondary electrons enter the interaction space after the primary electrons are switched, in Model B, most of them are trapped due to an effect called as magnetic mirroring. While in the case of Model C, the loss due to interception of secondary electrons at the anode is much more pronounced compared to Model A and B. We shall study these differences in detail in subsequent chapters for the three different model types using static and time-domain simulations.

Chapter 2: Model A: Uniform magnetic field with no beam compression

Model A is the simplest configuration that we consider, it allows us to explore the basic operating principles of the device. Model A as shown in Fig. 5(a) has a uniform and constant magnetic field (0.1T) to guide the electron beam from the emitter maintained at -70kV ($-V_{AK}$) to the collector. The area of the cathode (8.32 cm^2) is selected to keep peak loading of thermionic cathode below 5 A/cm^2 (see, e.g., Ref. [12-13]), the emitter width has been designed such that for a 30 A beam current the peak cathode loading is about 3.4 A/cm^2. The average loading will depend on the selected pulse width. It can be anticipated to be a factor of 4 – 8 smaller than the peak loading. The separation between the emitting surface and the mod-anode is 2 mm. This separation was chosen to give an adequate clearance between emitter surface and the mod-anode while also keeping the voltage swing as low as possible (the difference between mod-anode voltages when beam is on and cut-off). With the emitting surface at -70kV, for a 30 A beam current we will require the mod-anode to switch from -68.75 kV (on) to -71 kV (cut-off), these values were found using the Michelle static-case simulation results for the model shown in Fig. 5. The anode and collecting surface are separated by the decelerating gap (15 mm). The Kilpatrick breakdown limit [14] for our frequency range 3-10 MHz varies from 40 kV/cm (for 3 MHz) to about 50 kV/cm. By increasing the radii of the rounded edges from 2.5 mm to 5 mm we can reduce the maximum electric field strength to well within the breakdown limit. The sharp edges also plays a deciding factor in transverse electron beam energy, thus further optimization of the design by rounding these edges also leads to reduction in transverse beam energy and a slight increase in efficiency of the design.

In this geometry the modulation anode needs to switch between $-V_{AK}$ + 1.25kV and $-V_{AK}$ – 1.0kV to achieve class D mode of operation. This level of voltage swing can be supplied by an inductive adder [18]. An inductive adder uses a method known as inductive voltage addition where drive circuits are connected in series and in a specific way to add their voltages while maintaining a rapid rise and fall time [19]. The inductive adder is formed by a series of N identical, cylindrically symmetric cells which are essentially 1:1 transformers. The secondary of each individual cells are connected in series, thus enabling for addition of voltages. One of the main advantages of the IVA is its modularity. It is possible to tailor the output voltages by layering several primary layers as shown in Fig. 4.

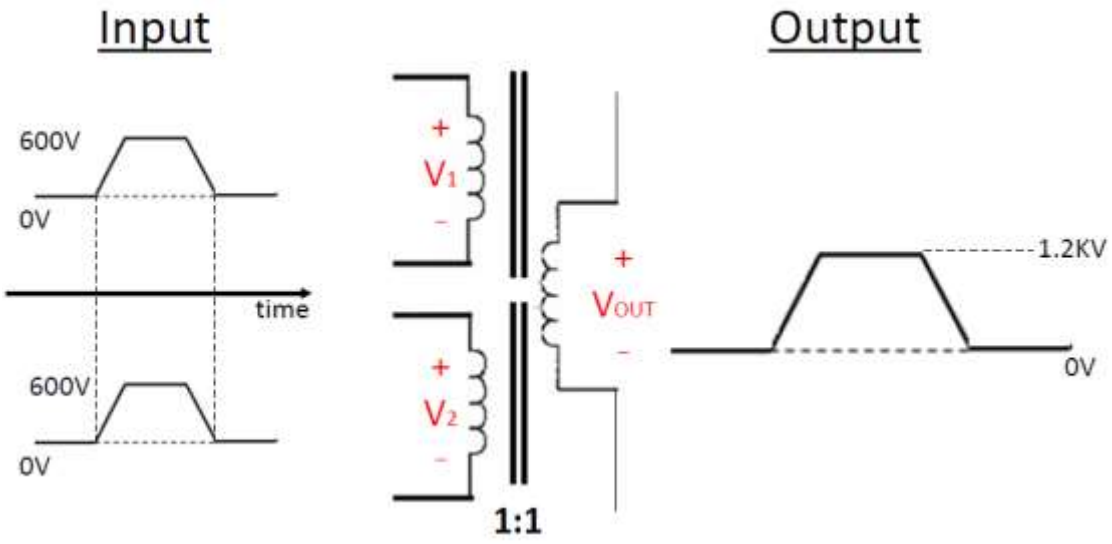

Fig. 4. A schematic drawing showing the basic principles behind Inductive Voltage Addition

The modulated beam is then accelerated toward a grounded anode. The beam is annular and thin so that electrons passing through the device experience nearly the same accelerating and decelerating fields. Electrons then pass a decelerating gap, across which the RF field is excited, and are collected by a collection surface. The DC potential of the collector is the same as that of

the anode (i.e. it is at 0 kV). However, the instantaneous potential on the collector varies sinusoidally in time with a peak negative value, $-V_{RF,\,max}$, that is close in magnitude to $-V_{AK}$, so as to fully decelerate the beam and extract all its kinetic energy. The collected current returns to ground through a resonant energy extraction circuit. Because the frequency of operation is low (3 – 10 MHz) and the electron transit time is short (less than 2 ns) the device can be basically understood as cycling at the RF period through a sequence of static equilibria. Thus, when the beam is "on" the collector potential is large and negative, and nearly all the beam kinetic energy is recovered by the collector. When the beam is "off", the collector potential swings positive, so that the time average potential at the collector is at ground. Since the collector potential oscillates at the RF voltage, the capacitance of the collector must be accounted for in designing the resonant extraction circuit.

2.1 Calculation of ideal operating point to obtain maximum efficiency

The electron beam propagation through the device is illustrated in Fig. 5 where we display the results of a Michelle simulation for the Model A configuration of the device. Shown in the figure are the path of the electron beam (on top) and the normalized momentum of the electrons ($p' = p / mc$) (below), as functions of their position in the device as they pass from cathode to collector.

For this simulation the RF voltage has been made as large as possible without reflecting any electrons. In this case I = 30A, V_{AK} = 70 kV and V_{RF} = 65.5 kV yielding an instantaneous efficiency of $\eta_I = 0.935$. It can be seen that some electrons nearly come to rest at z = 0.14 m

before striking the collector. The slight increase in the momentum in the vicinity of the collector is due to the suppression of the space charge field near the metallic surface of the collector.

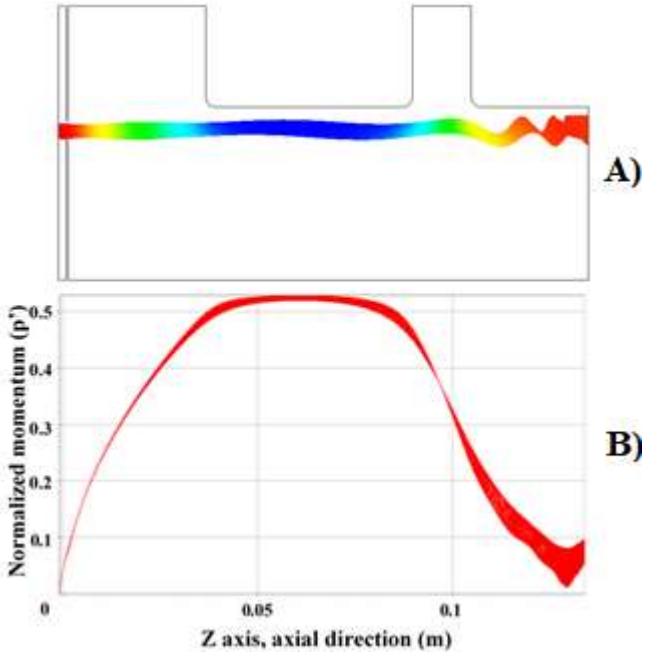

Fig. 5. a) Model A with uncompressed beam current of 30 A guided by a constant uniform magnetic field of 0.1 T (the wall radius is 4.4 cm and the outer and inner radii of a annular electron beam before the gap are 4.0 and 3.6 cm, respectively); b) The distribution of the normalized electron momentum when decelerating voltage is maximum (no reflected electrons)

The difference between the cathode potential and the RF voltage $V_{SC} = V_{AK} - V_{RF,\max}$, is due to space charge primarily in the region near the collector where the decelerated beam is slow. In subsequent sections we consider several variations of the configuration shown in Fig. 5 aimed at reducing this potential V_{SC}. For now we make the reasonable assumption that in high efficiency regimes the potential V_{sc} is rather small and therefore this potential can be described by a collector perveance μ_c such that

$$I = \mu_c V_{SC}^{3/2} \tag{5}$$

The collector perveance, μ_c, depends on the geometry of the beam: its thickness and proximity to conducting walls and on the strength of the confining magnetic field. For the device pictured in Fig. 5, we obtain V_{SC} = 4.5 kV and $\mu_c = 99.4\times10^{-6}$ from Michelle static-case simulation. For now we will take the perveance to be a given constant and consider the consequences. We can introduce $I_{?\mu} = \mu_c V_{AK}^{3/2}$ and estimate dependence of the maximum instantaneous efficiency on current to be

$$\eta_{I,\max} = \left(1 - \frac{V_{SC}}{V_{AK}}\right) = \left(1 - \left(\frac{I}{I_\mu}\right)^{2/3}\right) \tag{6}$$

We can now evaluate the average efficiency according to Eq. (3), and plot its level curves in the plane of $2\theta = \omega T$ and $I_{?}/I_\mu = I/(\mu_c V_{AK}^{3/2})$. Such a plot appears in Fig. 6.

We now adopt the approach that there is a minimum acceptable efficiency, and we wish to choose the "on" phase duration and peak beam current to maximize output power at fixed beam voltage. That is, we wish to move along a constant efficiency curve in Fig 5 until we find the point at which power is maximized. In moving along the constant efficiency curve variations in peak current and "on" phase are related as follows from Eq. (3):

$$\frac{\delta\bar{\eta}}{\bar{\eta}} = \frac{\delta I}{I}\left(\frac{I\, d\eta_{I,\max}}{\eta_{I,\max} dI}\right) + \frac{\delta\theta}{\theta}\left(\frac{\theta\, d\eta_\varphi}{\eta_\varphi d\theta}\right) = 0 \tag{7}$$

Since we are moving along a constant efficiency curve at fixed beam voltage, maximizing power is equivalent to maximizing average beam current. Average beam current is proportional to the product of peak beam current and "on" phase. Thus, the maximum power occurs when

$$\frac{\delta I}{I}+\frac{\delta\theta}{\theta}=0 \tag{8}$$

Performing the indicated differentiations in Eq. (7) on the functions defined in Eq. (4) and (6), and using Eq. (8) allows one to find the optimum peak beam current as a function of "on" phase,

$$\frac{I}{I_\mu}=\left(\frac{\Psi}{1+\Psi}\right)^{3/2} \tag{9}$$

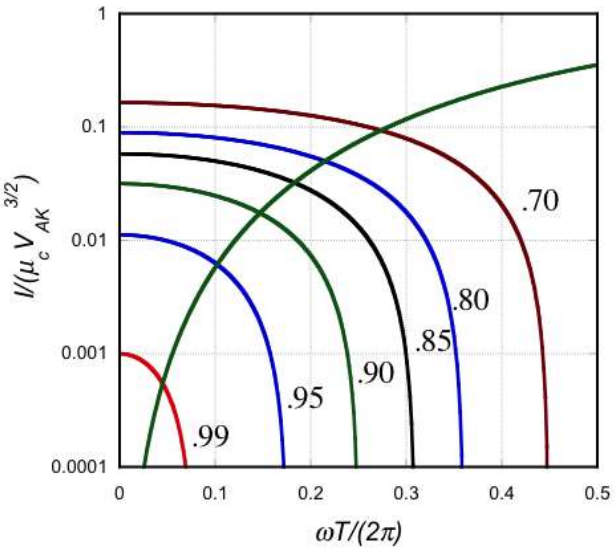

Fig. 6. Level curves of constant efficiency in the micro-pulse duration – peak beam current plane. The green curve intersecting the level curves is the locus of points where efficiency is maximized under the constraint of fixed average beam current

where $\Psi(\theta)=(3/2)[1-(\theta)\cot(\theta)]$. This curve is plotted in Fig. 6 as a solid green line that cuts across the level curves of efficiency. For a device with average efficiency equal to 90 %, the optimum operating point is $\omega T/(2\pi)=0.15$ and $I/I_\mu=0.017$. For the device pictured in Fig. 5 with operating voltage 70 kV and collector perveance $\mu_c=99.4\times10^{-6}$, the optimum peak

current is then 31.3 A, and the average output power is $\overline{P}$= 300 kW. We can also use these numbers to determine the gap resistance required to provide the correct decelerating potential, $R_g = |V_{RF}|^2 / 2\overline{P} = 7.15k\Omega$. Note that the emitter area is such that in the case of a 30 A beam current the cathode loading, as mentioned above, is about 3.4 A/cm^2. So, when the desire to shorten the current pulses requires utilizing higher peak currents this can be realized to some extent within conservative limit of 5 A/cm^2 or lower. In the case of approaching this limit, we have the freedom of enlarging the emitter cross-section, i.e. the beam thickness.

2.2 Static case simulations

Since the electron transit time is much shorter than the RF period, it is possible to carry out studies assuming that the RF voltage remains constant during the electron transit time (so-called 'static simulations'). A sequence of static simulations, with varying V_{RF}, is then carried out to determine the performance of the device as a function of time. In static simulations, for electrons emitted from the cathode at the potential $-V_{AK}$, collected at collector at potential $-V_{RF}$, and passing through the power extraction circuit to ground, the ratio V_{RF} / V_{AK} defines the instantaneous electronic efficiency of the device. The electronic efficiency is then determined by averaging the instantaneous efficiency over the period of an RF cycle for which the beam is on.

2.2.1 Electron beam characterization

In order to better understand how to increase the RF decelerating voltage while avoiding reflecting electrons, we examine the distribution of momenta for electrons at several axial

positions for Model A. The electron momentum distribution is computed using the code Michelle and momentum values are recorded at the axial position values labeled in Fig. 7.

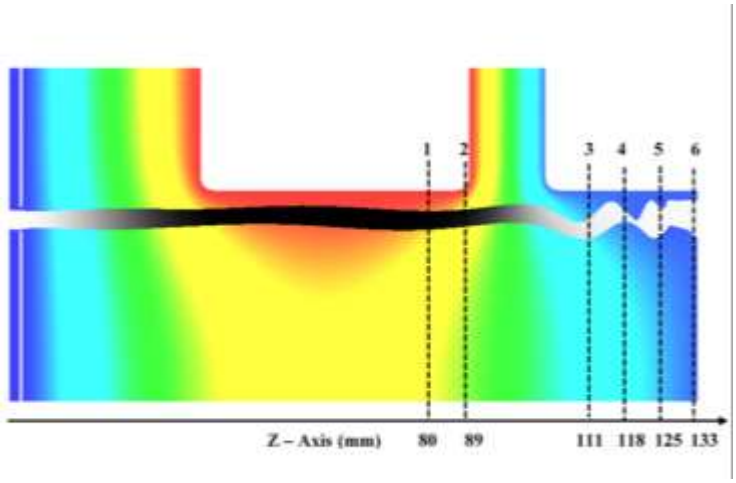

Fig. 7. A color map of the potential in the IOT with an electron beam. The potential field and electron distribution had been calculated across 6 different cross-sections numbered from 1 to 6

Using the data we made histograms of the total energy, $E_T / mc^2 = \sqrt{1+p_z^2+p_\perp^2}-1$ and surrogates for the axial and transverse contributions to the energy, $E_z / mc^2 = \sqrt{1+p_z^2}-1$ and $E_\perp / mc^2 = \sqrt{1+p_\perp^2}-1$. Here the momenta are normalized to *mc*, and we note that only in the nonrelativistic limit does $E_T = E_\perp + E_z$. These histograms are displayed In Fig. 8, for three of the locations designated in Fig. 7.

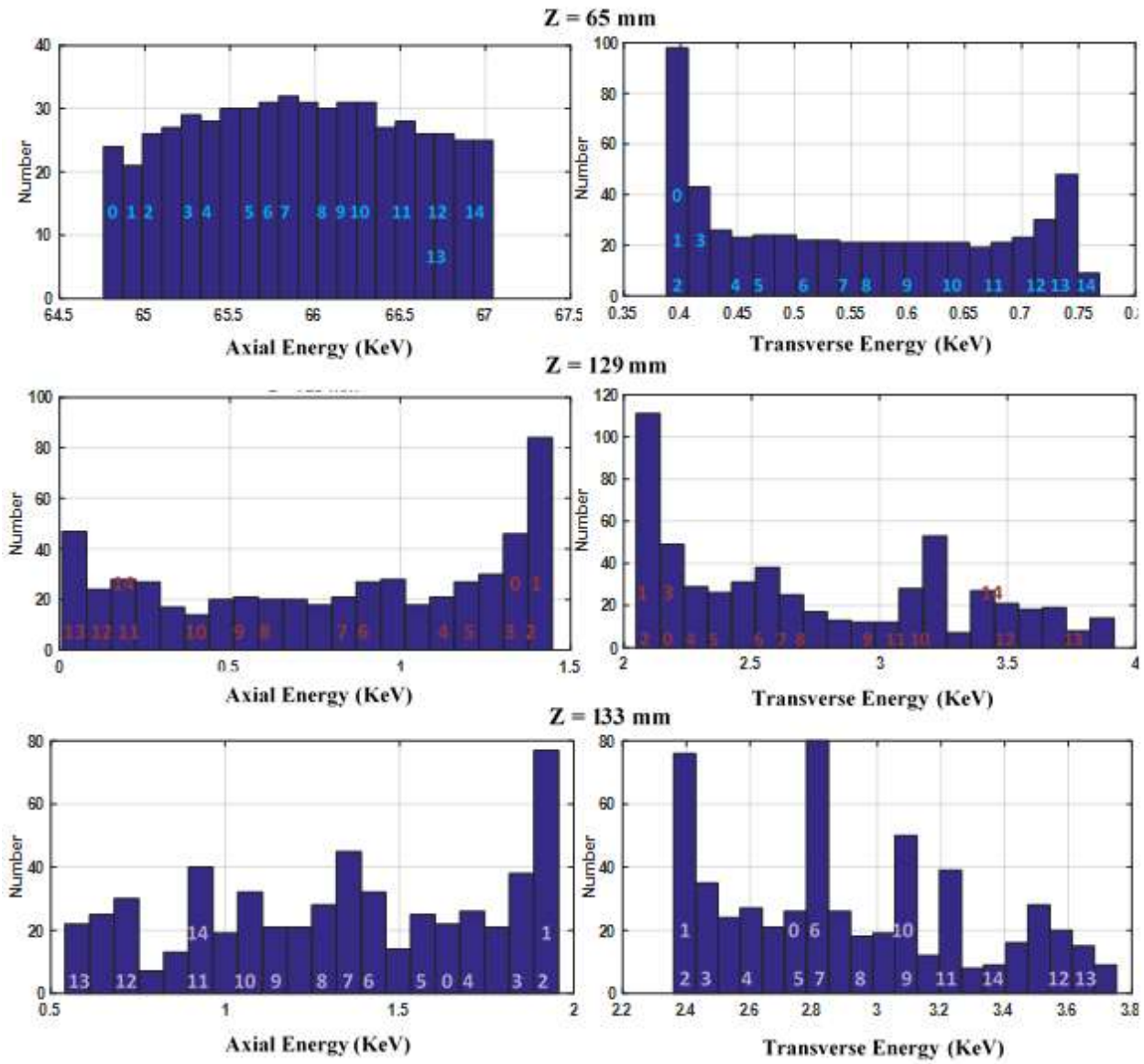

Fig. 8. Energy histogram showing the energy spread before and after the decelerating gap. The upper row shows the histograms of the axial (left) and perpendicular (right) kinetic energies before the gap (z=65 mm). The middle row shows such histograms in the cross-section z=129 mm where the axial momentum is minimal and, hence, this cross-section is the most prone to appearance of reflected electrons. Two figures on the bottom show similar histograms in the vicinity of collector (z=135 mm)

The histogram data in Fig. 8 shows that before the gap the energy associated with the axial motion greatly exceeds the energy associated with transverse motion as expected. The deceleration of the beam electrons by the RF field in the gap greatly reduces the axial energy,

while increasing the transverse kinetic energy. So, after deceleration, the average transverse kinetic energy exceeds the axial energy by almost a factor of three. This increase in transverse energy is responsible for reducing the maximum value of the RF voltage that does not cause electron reflection. The fact that the energy associated with the transverse motion greatly exceeds the axial energy complicates the use of the perveance introduced in Section **2.1**. A constant perveance assumes that as current and potential are varied, electrons follow the same trajectories through space, only changing their speed. This is a good approximation if the magnetic field is strong, such that the product of the cyclotron frequency and the transit time from the gap to the collector is greater than unity, but it does not hold as we will show when the magnetic field is weaker. The histograms of the total kinetic energy near the collector are shown in Fig. 9. The mean kinetic energy is about 66.9 keV consistent with the instantaneous efficiency of 95.6%.

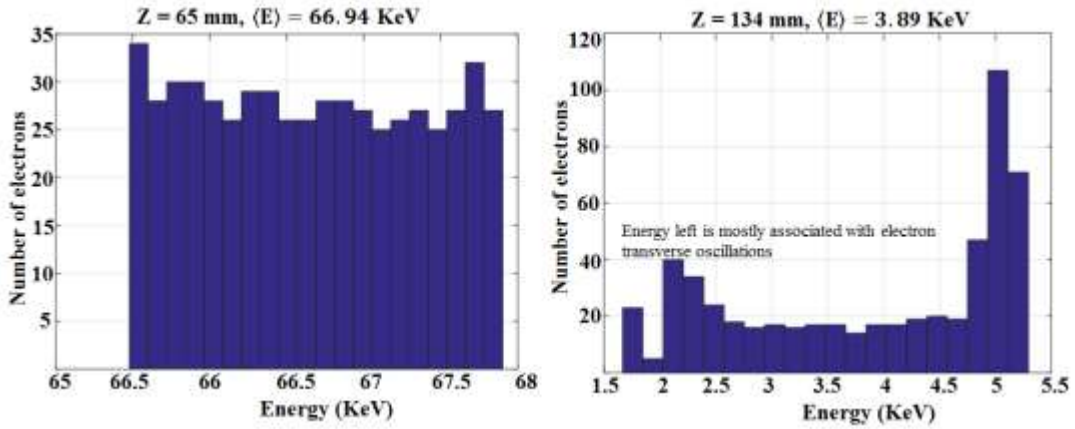

Fig. 9. Energy histogram showing the total kinetic energy spread of the beam particles before (left) and after the decelerating gap (right)

Fig. 10 displays numbered simulation beamlets as they emerge from the cathode. These numbers are also displayed on the histograms in Fig. 8. As one can see in Fig. 8, the innermost electrons 1 and 2 have the lowest axial energy before the gap because for them the clearance from the wall is maximal and, hence, the potential depression is strongest. However, after the

gap, the outer electrons, which were decelerated stronger than others, have the lowest axial energy, while the innermost electrons have the highest axial energy and, at the same time, the lowest transverse energy because their motion was perturbed by the space charge field not so strongly.

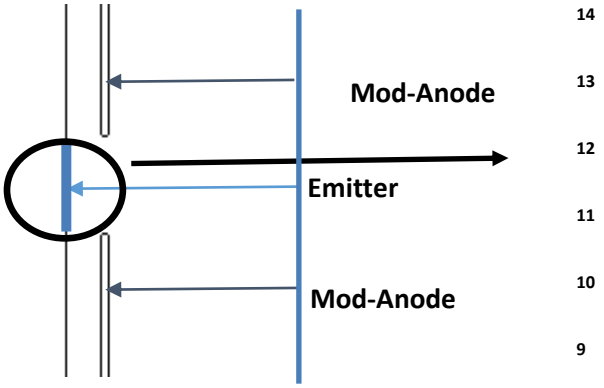

Fig. 10. Emitter, location of the chosen sites there and their radial coordinates

Let us now return to Fig. 7 and consider radial distribution of the potential within the electron beam and its vicinity in 4 out of 6 cross-sections shown in Fig. 7, i.e. in the cross-sections after the gap. This distribution is shown in Fig. 11. This distribution becomes more and more uniform as electrons approach the metallic collector wall. The smoothening of the potential profile corresponds to the shape of the collector (flat surface as shown in Fig. 7). It is also interesting to note that the potential falls below the collector potential (z = 125 mm) due to buildup of space charge near the region where the electron beam strikes the collector surface.

We were thus able to characterize the beam dynamics by studying the static-case energy histogram at different z-axis location of the device. The particle dynamics of the electrons located at the inner most edge of the beam (closest to the anode wall) is quite different compared

to those at the outermost edge due to space charge effects. We were also able to show the reduction in potential due to space charge effect near the collecting surface as seen in Fig. 11.

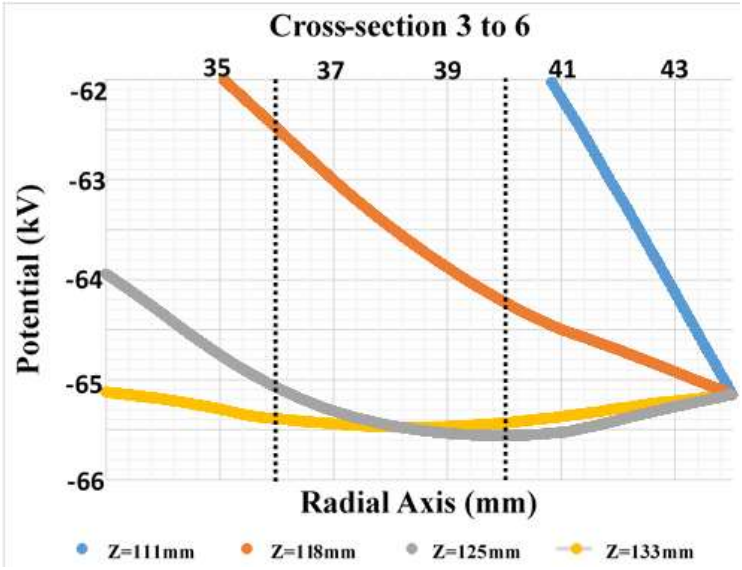

Fig. 11. A detailed plot of the potential evolution from the cross-section 3 to 6 (z=111 mm to z=133 mm)

2.2.2 Collector design as a static case problem

There are two issues that must be addressed with regard to the configuration of the collector in our device. The first is the impact of collector design on instantaneous efficiency. As the electron beam is decelerated and approaches the collector, some electrons may be reflected due to the space charge electric field and the buildup of transverse energy. Avoiding this determines the maximum decelerating voltage and efficiency. We will address this by looking at several different collector configurations. The second issue is the potential problem of an excessive local heat load on the collector due to the distribution of electron impacts on the collector. This will be examined by considering a collector with a tapered wall radius to spread out the region where the beam strikes the collector.

Length of separation (mm)	**V_{RF}[kV]**	**Efficiency (%)**
27.5	65.15	93.07
22.5	65.5	93.57
17.5	65.75	93.92
12.5	65.95	94.21
7.5	66.125	94.46
0	66.775	95.39

Table 2. The effect of the separation between the collector and decelerating gap

As shown in the configurations in Fig. 5 and 7, electrons propagate a distance of 27.5 mm after the gap before striking the collector. We therefore varied this distance by moving the collector plate closer to the gap. It is shown in Table 2 that the device efficiency (2) increases as this distance is shortened by more than 2%.

Figure 12 illustrates the electron motion and axial dependence of the electron momentum in the limiting case where the collector plate is located in the same cross-section as the end of the gap. In this case there is no electron re-acceleration in the vicinity of the collector as seen in Fig. 5. There is still transverse motion in the beam as it approaches the collector due to the fact that the beam has experienced some transverse perturbations on its trip from the cathode to the collector. This particular design uses a simple flat wall collector to study the effect of space-charge on electron deceleration in the gap region and on electron motion in the vicinity of the collector. A more realistic collector configuration is discussed below.

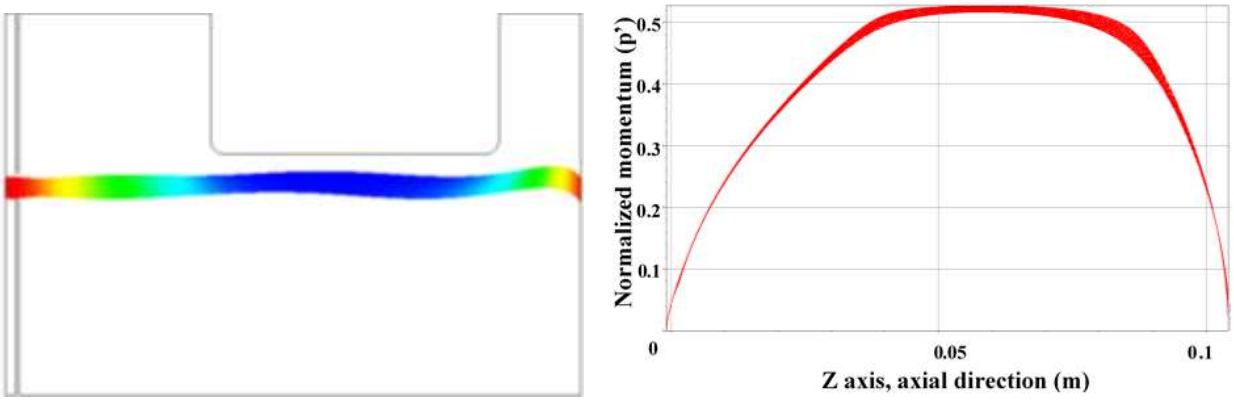

Fig. 12. A perpendicular collecting surface with lowest separation from the decelerating gap

Effect of guiding magnetic field: The simulations performed for the configuration shown in Fig. 12 (where electron trajectories are shown for a 0.1 T magnetic field) were also performed for 0.15 T. This increase in the focusing field resulted in significant suppression of electron transverse motion. Correspondingly, the maximum RF voltage in the case of a 30 A beam increased from 66.775 kV (for 0.1 T) to 69.35 kV (for 0.15 T). This corresponds to the increase of the instantaneous efficiency from 95.39% to 99.07%. It was also found that with this higher magnetic field the current dependence of the instantaneous efficiency was consistent with a constant perveance as assumed in Eq. (6).

The downside of this simple design is the high power density striking the collecting surface. In the absence of an RF field, the peak power of a 70 kV, 30 A electron beam is 2.1 MW, while the cross-section area of the annular beam is about 9 cm^2. When the beam pulse duration is a quarter of the RF period the mean value of the beam power density is 55 kW/cm^2. Even in the case of operation with 90% efficiency, the power density is still above 5 kW/ cm^2, which is unacceptable for high average power regimes.

To reduce the beam power density to an acceptable level (less than 500 W/cm^2), we considered a slanted collector surface with an angle of 6 degrees or less with respect to the device axis. An

example is shown in Fig. 13 where the angle is 4.3 degrees, the resulting efficiency is 93.9%, and the beam power density is less than 500 W/cm^2.

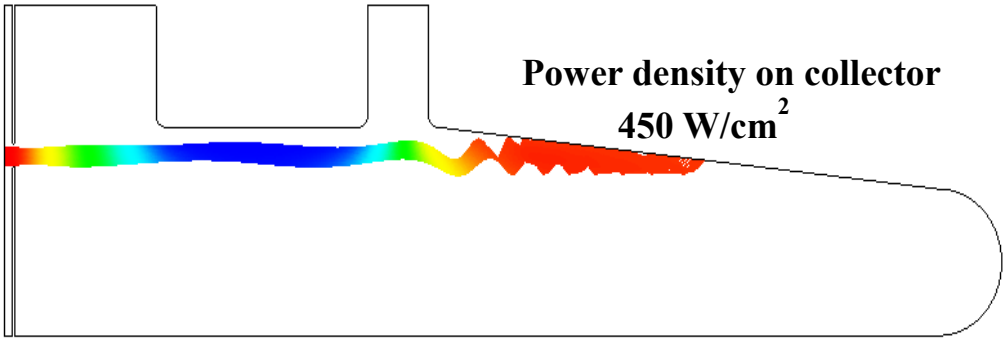

Fig. 13. A slanted collector surface. There is a slight loss in efficiency compared with the perpendicular collecting design, but the power density striking the surface is well within acceptable limits. The maximum decelerating voltage is 65.75 kV for a 30 A beam current

2.2.3 Effect of electrode geometry

The ratio V_{RF}/V_{AK} defines the instantaneous efficiency, the closer V_{RF} is to V_{AK} the higher instantaneous efficiency. However, the RF voltage is limited by the fact that we want all beam electrons to reach the collector. Electrons will be reflected if they acquire too much transverse energy on their passage from the cathode through the gap, or if their space charge lowers the potential near the collector by a large amount. The electrode geometry determines the maximum achievable V_{RF} and instantaneous efficiency. Depending on the geometry it is possible to reduce the transverse energy gained by the beam electrons and shield their space charge, and thus maximize the RF voltage.

Two different anode geometries were considered: (a) an anode with sharp corners and (b) an anode with rounded corners (7.5 mm radius of the rounding). An example of the configuration

with a rounded anode is shown in Fig. 14. The collector geometry is kept fixed, while the length of the AK-Gap and the length of the anode were varied.

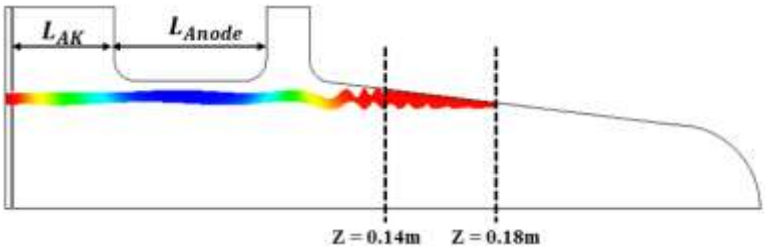

Fig. 14. Beam trajectory obtained from static simulation. The anode edges are rounded (7.5 mm radius of the rounding), with L_{AK} = 37.5 mm and L_{Anode}= 52.5 mm. The electron beam strikes the collector first at Z = 140 mm and ends at Z = 180 mm

Table 3 displays the maximum instantaneous efficiencies for devices with different dimensions. In Table 3, the anode length is varied with AK gap length fixed at 37.5 mm. In Table 4, the AK gap length is varied with anode length fixed at 27.5 mm. Our goal is to decrease the overall length of the device while maintaining high efficiency. After multiple simulations, it was concluded that an anode length of 27.5 mm and an AK gap length of 32.5 mm are the optimal lengths. The maximum RF-voltage (V_{RF}) for such a device is 65.75 kV with a 94% instantaneous efficiency. The reason for the high efficiency is that the electrons are in a thin annular beam and propagate with a small radial distance (4 mm) of the anode. Thus, they gain little transverse energy while transiting the device and are collected at a potential close to that of the cathode. It should also be noted that the maximum RF voltage is quite sensitive to modifications in the AK-Gap length, especially when this length is shorter than 32.5 mm. This is due to the fact that reducing the AK-Gap length leads to an increase in the transverse component of the electron momentum as a result of the radial component of the electric field from the edges of the mod-anode and anode. Adding transverse momentum to the beam electrons reduces their axial momentum and lowers the potential at which they can be collected.

$L_{anode}(mm)$	$RF_{Rounded}(kV)$	$\eta_{Rounded}(\%)$	$RF_{Sharp}(kV)$	$\eta_{Sharp}(\%)$
52.5	**65.75**	**93.9**	**65.25**	**93.2**
40	**65.75**	**93.9**	**65.25**	**93.2**
27.5	**65.75**	**93.9**	**65.25**	**93.2**
20	**64**	**91.7**	**63.75**	**91**
15	**63.75**	**91**	**63.25**	**90.4**

Table 3. RF voltage and its relation to AK-gap and Anode length (No secondary electrons). The anode length is varied while keeping the AK-gap length fixed at 37.5 mm

$L_{AK}(mm)$	$RF_{Rounded}(kV)$	$\eta_{Rounded}(\%)$	$RF_{Sharp}(kV)$	$\eta_{Sharp}(\%)$
37.5	**65.75**	**93.9**	**65.25**	**93.2**
32.5	**65.75**	**93.9**	**65.25**	**93.2**
30	**65.5**	**93.6**	**64.75**	**92.5**
25	**62.75**	**89.6**	**62.5**	**89.2**
20	**60.75**	**86.8**	**60.75**	**86.8**

Table 4. RF voltage and its relation to AK-gap and Anode length (No secondary electrons). The AK-gap length is varied while keeping the anode length fixed at 27.5 mm

This is more pronounced in the case of sharp edges since such surfaces produce potential contours which change rapidly compared to those produced by smoother edges. The results obtained from the static-case simulation guide the computations presented in the next section when the role of secondary electron is studied, where we investigate the secondary electron dynamics for both the long model (AK-gap length = 37.5 mm and anode length = 52.5 mm) and the compact model (AK-gap length = 32.5 mm and anode length = 27.5 mm).

2.3 Time- Domain simulation

2.3.1 Secondary electrons and the physics of their interaction

When primary beam electrons strike the collector surface, they are not all absorbed by the metal, some fraction of electrons are scattered and reflected and these electrons are called as Backscattered electrons (BSE). A fraction of primary electrons striking the surface can generate new “secondary” electrons via ionization, these electrons are called as secondary electrons, and their presence can affect device operation. Once the secondary and reflected electrons are included in the computations, we have to switch from static simulations to the time-domain simulations. The behavior of these secondary electrons depends on the time within the RF cycle. That is, the behavior depends on whether the primary beam current is on or off.

As in the previous section, we assume that the magnetic field is uniform along the axis. So, secondary and reflected primary electrons can propagate back into the interaction space during the positive cycle of the RF voltage. The time evolution of the RF voltage and the beam current are shown in Fig. 15. The beam current is switched on at $t = 13\ ns$ and switched off at $t = 27\ ns$. The electrons take roughly 1.5 ns to travel from the emitter to the collector.

Figure 16 shows the axial momentum and total transverse momentum obtained at two different times during the on period of the beam current, 20 ns and 26 ns. The simulations are done for the AK gap distance of 37.5 mm and the anode length of 52.5 mm.

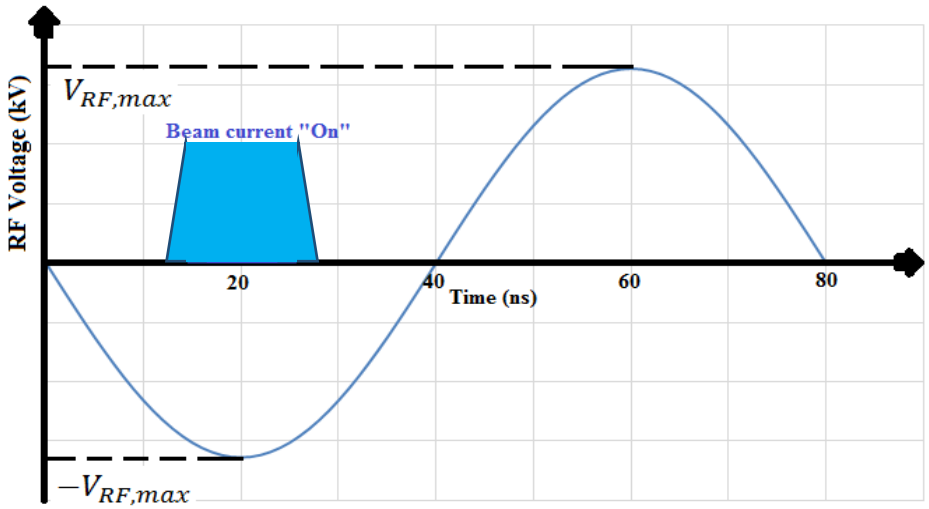

Fig. 15. Plot showing the RF voltage and beam current dynamics during one full cycle

As seen in Fig. 16a and 16c, (at $t = 20\ ns$ and $26\ ns$, respectively) the primary beam, emitted from the cathode (shown in green), is accelerated in the AK-gap. The beam then travels past the anode with small change in axial momentum until it encounters the decelerating gap. The decelerating RF field, extending a distance on both sides of gap region, reduces the axial momentum of the beam, which then travels to the collector. Figures 16b and 16d show the transverse component of the momentum plotted over the same axial distance. The transverse momentum increases as the beam passes through the gap region as a result of the transverse component of the RF field. The energy associated with this transverse motion then limits the maximum RF voltage. The figures are similar, indicating that the behavior of the electrons during the flat-top portion of the current pulse is also similar.

Note from Fig. 15 the RF voltage is different at these two times. When the decelerated primary beam strikes the slanted collecting surface it produces secondary electrons. Here red, black, and pink colors indicate first, second and third generation secondaries. It is also important to mention that adding further secondary generations in the simulation does not change the axial and transverse momenta profile of the electrons. The secondary electrons are separated into different groups having different momenta and spatial locations. Further, there is a group of relatively low energy secondary electrons in addition to secondary electrons with higher energy and positive axial momentum taking them in the direction of the collector.

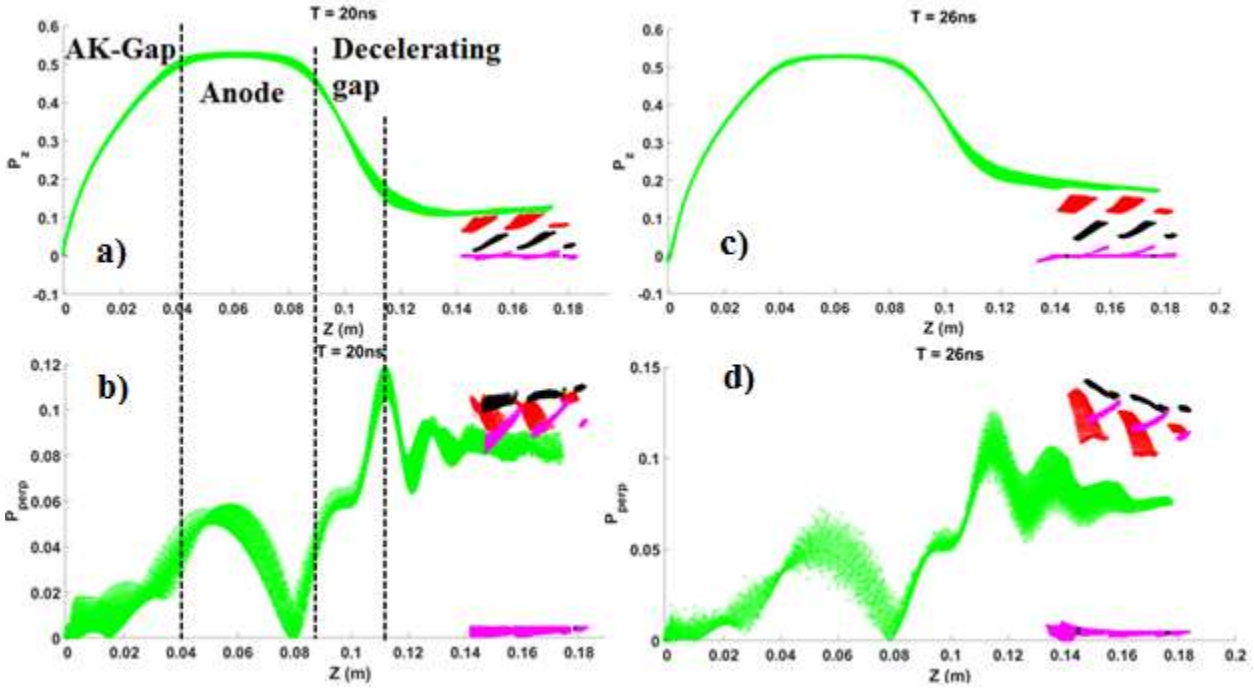

Fig. 16. Axial (a) and (c) and transverse (b) and (d) momenta of primary and secondary electrons at t = 20 ns and t = 26 ns. Primary electrons are shown in green, the first generation of secondaries (red) gives birth to the second generation (black) which in turn produces the third generation of secondaries (pink)

The slow moving secondaries have almost zero axial and transverse momentum. These secondary electrons, produced close to the decelerating gap, are susceptible to the RF field,

which could accelerate them back into the gap. However, these slow moving secondary electrons are unable to leave the collecting region when the primary beam is present due to the space charge of the primary electrons that creates a potential barrier keeping them near the collector. This will change later in the RF cycle, when the primary beam is off.

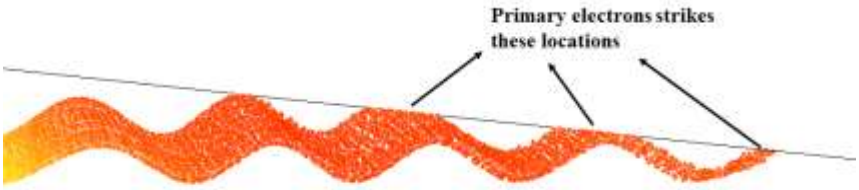

Fig. 17. Primary electrons strike the slanted collector at three different locations. Note: Secondary electrons are not shown in this figure but are shown in Fig.18

As follows from Fig. 16, the secondary electrons can be separated spatially into various groups. This separation is the result of the gyration of the primary electrons as they approach the collector. The primary electrons strike the collector at three different locations as shown in Fig. 17. The secondary electrons generated are thus also separated spatially into three different groups, as shown in Fig. 18.

A spent beam of primary electrons is represented by a set of energy-modulated macro particles. For taking into account the role of energy and incident angle distribution of the primaries in the production of secondaries, a comprehensive secondary emission model [20] is included in the code. The high-energy secondaries are essentially primary electrons that have been scattered out of the metal collector. They have positive axial momenta, and hence, can generate new secondary electrons; each subsequent generation shifts to the right. However, this shift is quite small since they also have large transverse momenta. The low energy electrons are true secondaries that have been produced in the collector by collisions with the primaries. These

electrons are produced in each generation. Only the third generation is visible in the figures as they are plotted last obscuring the earlier generations.

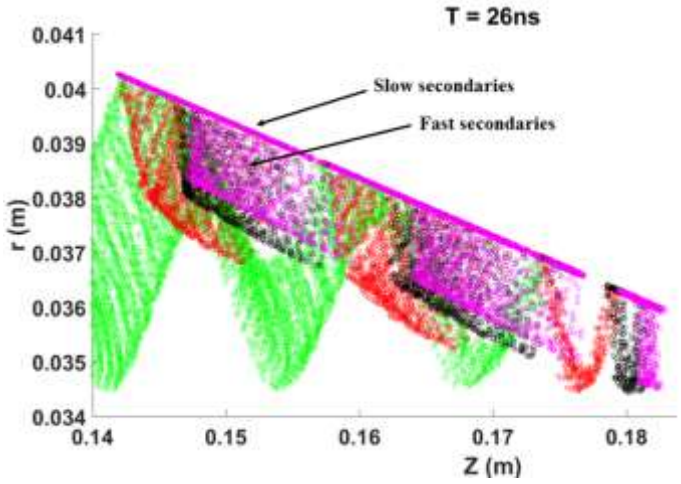

Fig. 18. Radial position of primary (green) and secondary (red, black and pink) electrons as a function of their axial position. The fast secondaries gyrate in a similar fashion to the primary electrons and strike the slanted collector at three different spots, with each subsequent generation being shifted to the right by a small amount

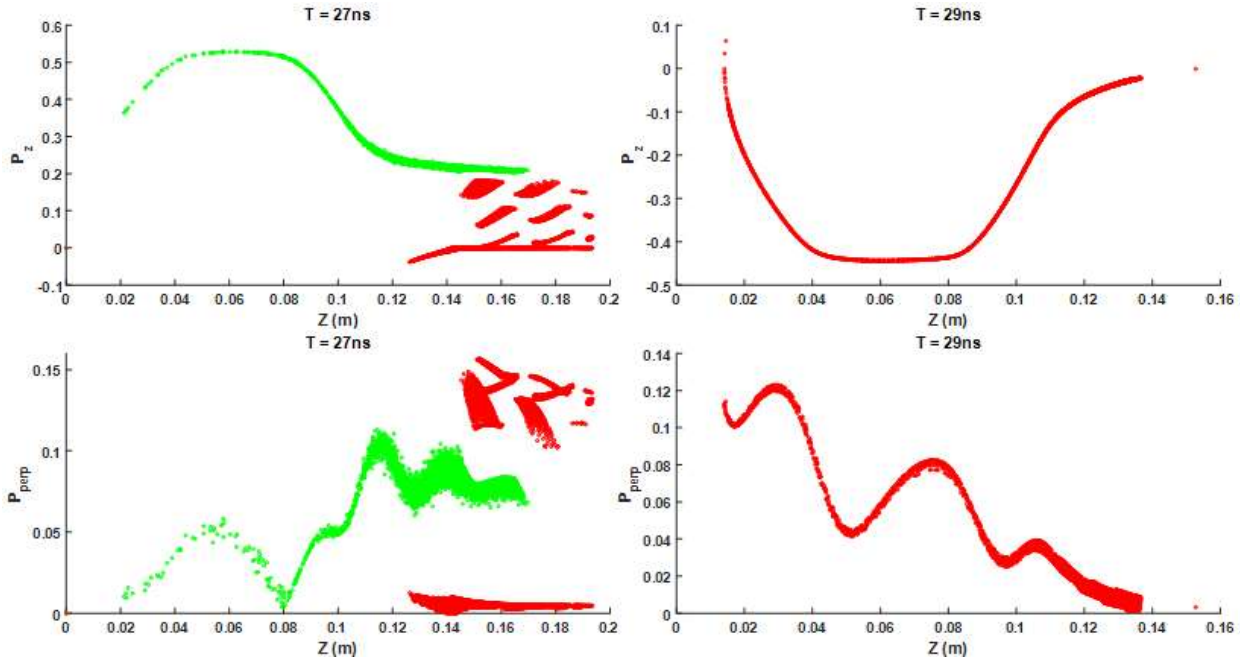

Fig. 19. Axial and transverse momenta distribution of primary (green) and secondary (red) electrons at t = 27 ns and t = 29 ns for the long version of the device (L_{AK} = 37.5 mm, L_{Anode} = 52.5 mm). **Note**: All secondary generations are shown in red

Once the primary beam current is switched off at $t = 27$ ns, the slow secondary electrons, which were previously confined in the collector area by the space charge field of the primaries, begin to escape from this region into the interaction space as shown in Fig. 19. As these electrons pass through the decelerating gap, they are now accelerated by the RF voltage in the negative z-direction until they reach the anode region and encounter the barrier created by the difference in potentials between the mod-anode and anode. These electrons are now trapped between two potential barriers and move back and forth in the interaction space.

In the long version of the device (L_{AK} = 37.5 mm, L_{Anode} = 52.5 mm) most of these electrons are intercepted by the grounded anode as shown in Fig. 20a. This process continues until about $t = 36$ *ns* when the RF voltage falls so that the barrier on the right becomes very low. Then, the electrons that were not absorbed by the anode can escape from the interaction space back into the collecting region where they are absorbed back into the collector.

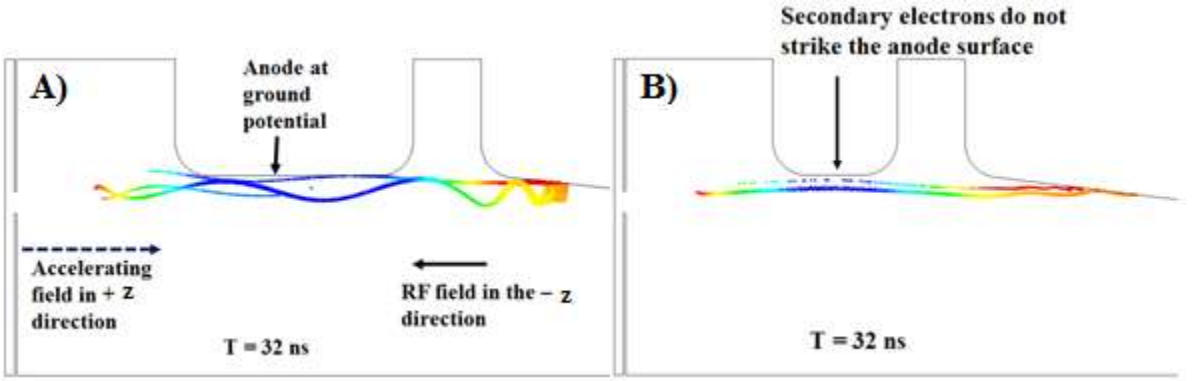

Fig. 20. a) A snapshot of the electron trajectories at t = 32 ns ($L_{AK} = 37.5\ mm, L_{Anode} = 52.5\ mm$), 4 ns after the primary beam current is switched off. The secondary electrons are absorbed at the grounded anode thus leading to a loss in efficiency. b) A snapshot of the electron trajectories at t = 32 ns ($L_{AK} = 32.5\ mm, L_{Anode} = 27.5\ mm$), 4 ns after the primary beam current is switched off. No loss in efficiency due to absorption of secondary electrons at anode

By the time the RF voltage changes sign at $t = 40$ ns (see Fig. 15), there are no more electrons (secondary or reflected) left in the device. The power contained in the secondary and reflected electrons accounts for roughly about 5.5% of the incoming beam power, the vast majority of which was absorbed into the anode as shown in Fig. 20a. This is disadvantageous since this reduces the device efficiency from roughly 93.9% to 88.4%.

The effects of reducing the AK-Gap and the anode length on RF voltage were presented in Section **2.2.3**. These simulations did not include secondary electrons and were static-case simulations. Then, we studied the relation between inclusion of secondary electrons and RF voltage in Section **2.3.1**, thus we can use the results shown in Table 3 and 4 while keeping in mind that inclusion of secondary electrons will likely reduce the RF voltage. Since the model being used for the time-domain simulation is the same compact model as that used in the static case simulation, the maximum RF voltage should likely still be within the range of 65kV. Taking these factors into account, the AK-gap length was reduced from 37.5 mm to 32.5 mm and the anode length from 52.5 mm to 27.5 mm. A snapshot of the particle trajectories at $t = 32$ *ns* is shown in Figure 8b. There is no loss in efficiency due to absorption of secondary electrons at the anode as seen in the other longer model (Fig. 20a).

There are several other ways to address the issue of efficiency loss due to interception at the anode. By increasing the magnetic field confinement from 0.1 T to 0.15 T it is possible to avoid interception at the anode (Static case analysis is presented in **2.2.2)**, however this will also increase the power consumption of the solenoid. Similarly, we can also increase the clearance between the beam and anode by increasing the anode radius. This however will make space charge effects stronger, thus reducing the maximum RF voltage and the device efficiency.

As shown in Fig. 21, the key features such as evolution of axial momentum, generation of slow and fast moving secondary electrons and clumping of secondary electrons into groups remain unchanged. However, the total transverse momentum does not fall to zero unlike in the longer device. This is due to the short anode length. The stronger transverse electric fields generated at the decelerating gap amplifies both radial and azimuthal components equally.

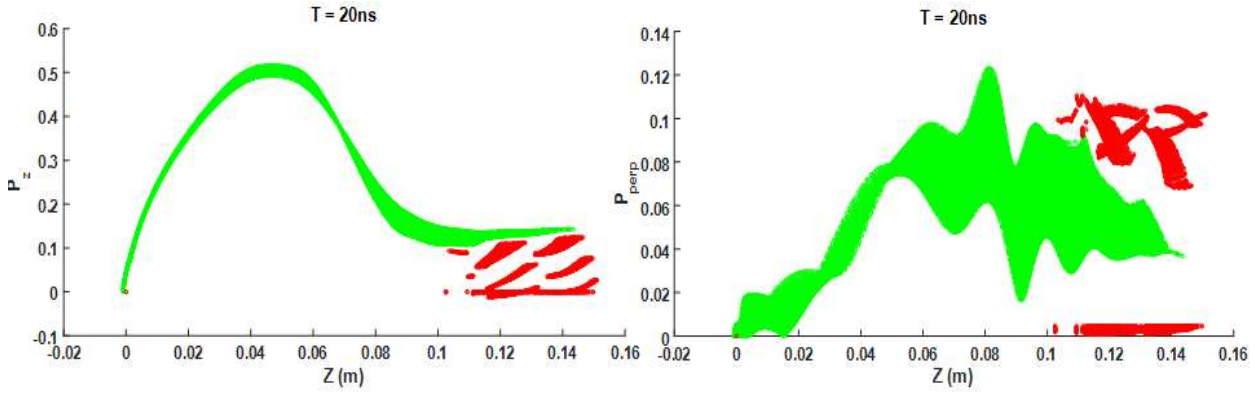

Fig. 21. Axial and transverse momenta distribution of primary (green) and secondary (red) electrons at t = 20ns for the compact model ($L_{AK} = 27.5mm, L_{Anode} = 32.5\ mm$). **Note**: All secondary generations are shown in red

2.4 Summary

The efficiency of a grid-less tetrode with constant magnetic field confinement (Model A) was considered. Maximizing average efficiency involves a trade-off between pulse duration and peak beam current as indicated in Eq. (3). The peak instantaneous efficiency depends on the beam current, magnetic field, and collector geometry. For sufficiently strong magnetic fields and flat collector surfaces the peak efficiency satisfies a scaling relation based on a geometry-dependent perveance as indicated in Eq. (6). However, for lower magnetic fields and for slanted collector surfaces, the efficiency depends less strongly on the current. In this case it is advantageous to operate with a high peak current and as short a beam pulse as possible. We were

able to optimize Model A device type by using Michelle static and time domain simulation results. The results were consistent with our theoretical predictions and we were able to obtain a high instantaneous efficiency of 93.9% and average efficiency of 91.5%. Overall system efficiency will also depend on the efficiency of the other subsystems. It may be the case that these factors limit the system efficiency and that further optimization of the electronic efficiency of the source is not needed.

In the next chapter we consider the more practical case with tapered magnetic field confinement. Due to the non-uniformity of the magnetic field and the radial beam profile we expect the efficiency to be lower than Model A. The lower efficiency is offset by various advantages such as smaller solenoid requirement and better secondary electron confinement in the collector region due to magnetic mirroring.

Chapter 3: Model B – Tapered magnetic field with non-uniform beam radius profile

The constant and uniform magnetic field used in Model A is an idealized field fed into the Michelle code via its inbuilt function. To actually produce the constant and uniform field we would require to build a large solenoid with at least twice the device length and an inner solenoid radius far larger than the device radius. Another option would be to use multiple smaller "pancake" solenoids, however such a composition would still end up being quite bulky. Thus the logical next step is to consider a device model with a magnetic field confinement generated by solenoids with lengths comparable or shorter than the device length. Such a device will have a non-uniform magnetic field and due to the short solenoid size varying beam radius profile.

In the case of Model A, we were able to use the Michelle code to provide a uniform constant magnetic field for beam confinement. However, this is not the case with Model B. The magnetic field profiling was done using Ansys Maxwell software in magnetostatic mode.

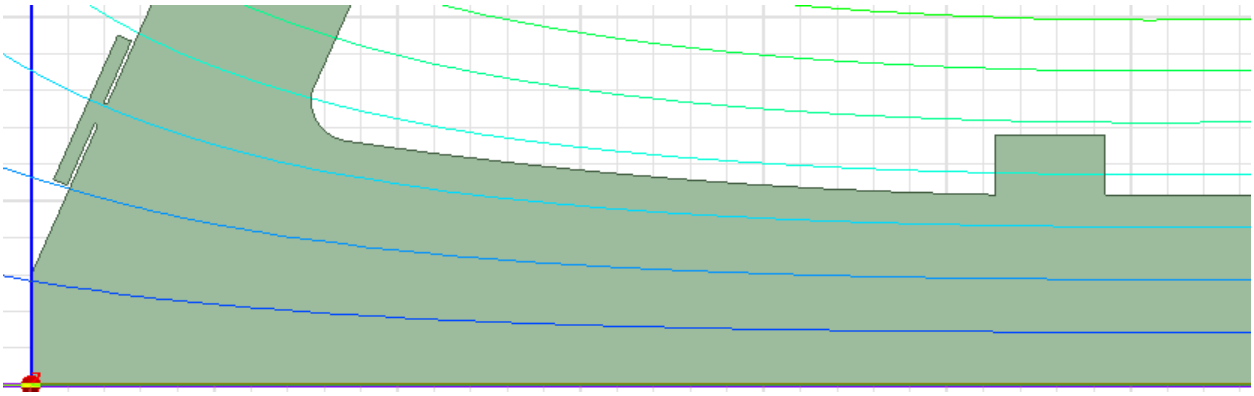

Fig. 22. Magnetic potential vector (A) lines of the confining magnetic field obtained from Maxwell

As we have discussed in Chapter 2, one of the important factors which limits the maximum decelerating voltage and device efficiency is the amount of transverse energy in the electron beam.

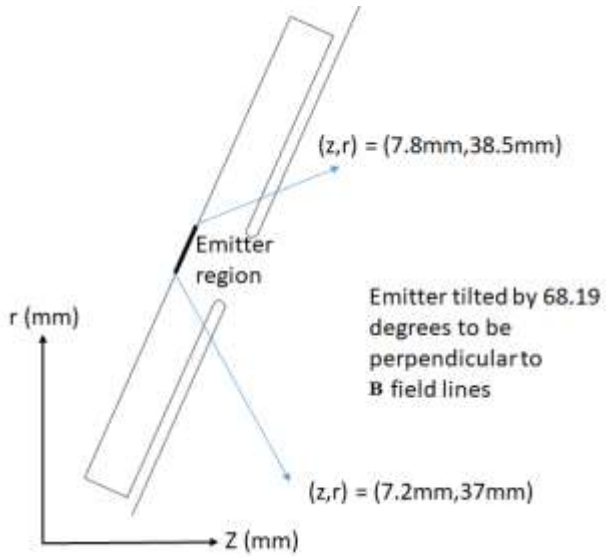

Fig. 23. An enlarged image of the emitter region. The emitting plane is tilted to be perpendicular to the immersed magnetic field lines

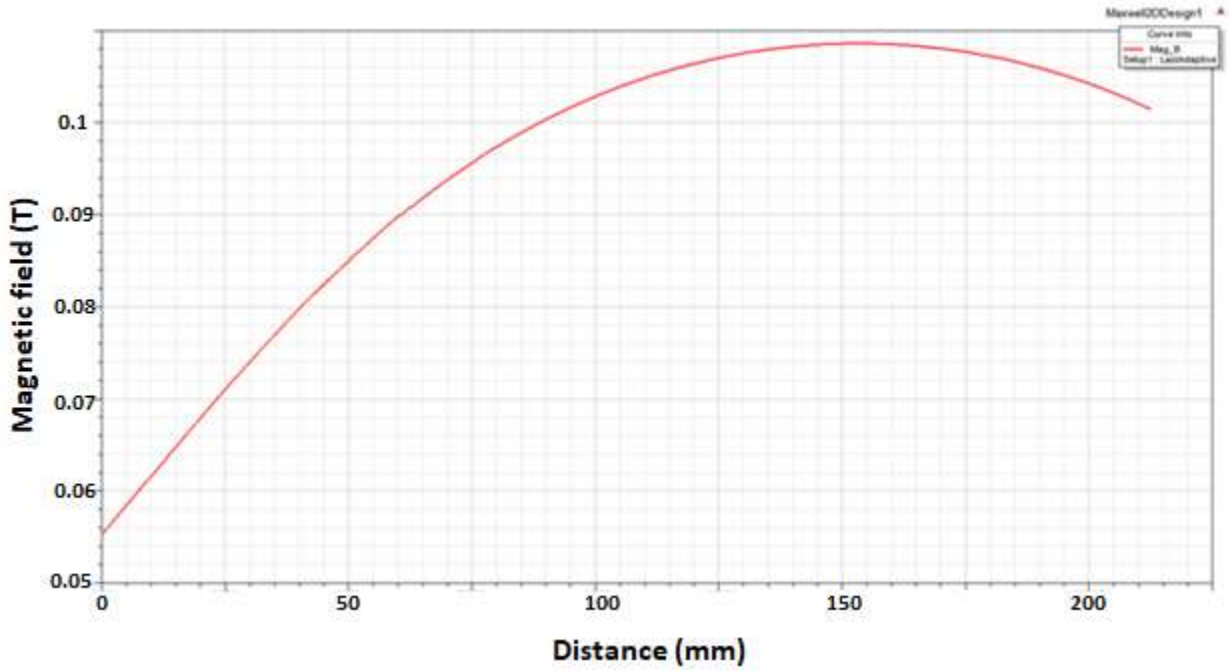

Fig. 24. Magnetic field magnitude along the electron trajectory. **Note**: The field has been scaled when exported to Michelle code so that the peak field value is 0.1 T

The electrons generated at the emitter are emitted perpendicular to the emitting surface and to ensure it doesn't pick any energy in the transverse component it is necessary ensure that we design the emitter to be perpendicular to the immersed **B** field lines as shown in Fig. 22 and Fig. 23. The magnetic field strength along the expected electron trajectories have been plotted in Fig. 24, the field was designed to have a peak value of 0.1 T at a distance of 150 mm from the emitter (or in other words, the electron beam experiences maximum magnetic confinement at the decelerating gap). The solenoid was placed in such a way that the electron beam experiences maximum magnetic field confinement as it approaches the decelerating gap.

3.1 Ripple factor and its effect on device efficiency

Figure 25 shows the electron trajectories of a 30 A beam current obtained from static-case Michelle simulation. The emitter was maintained at -70 kV while the mod-anode is maintained at -68 kV.

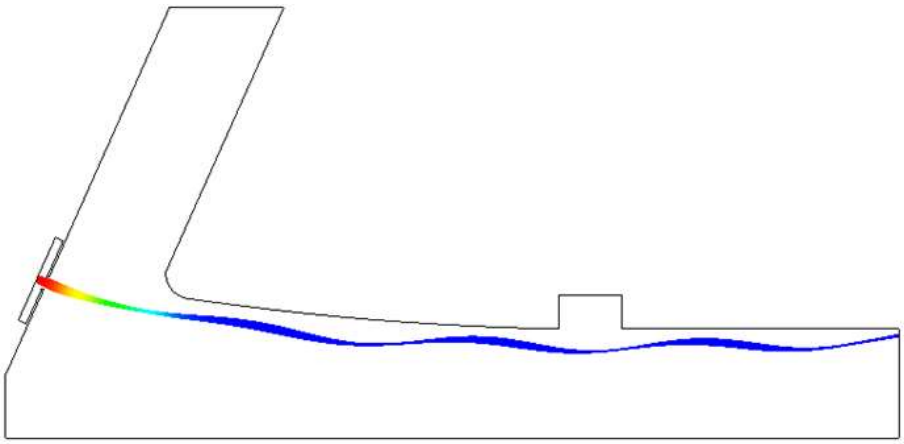

Fig. 25. The electron trajectories of Model B design obtained using static-case simulation

As shown in Fig. 25, the beam thickness is not uniform. We define ripple factor as the ratio of the maximum beam thickness and emitter length (this corresponds to the thickness of the beam right after generation at the emitter). The ripple factor is helpful since it gives us an idea of the amount of transverse energy in the electron beam. It is therefore possible to maximize device efficiency by reducing the ripple factor to as close to its theoretical limit of 1.

It will be quite useful to study the underlying cause behind these beam ripples. Let us study the potential contour plots shown in Fig. 26, the electron trajectories are dictated by the electric field generated between the emitter surface and mod-anode surface. Due to the difference in potential and the shape of the opening between the two surfaces we observe a diverging electrostatic lensing effect. It is possible to reduce this by increasing the distance between emitter and mod-anode, however this will have a large impact on the voltage difference needed between these two surfaces to generate a 30 A beam current. For a 30 A beam current to be produced for a separation of 2 mm between the two surfaces, the mod-anode has to be maintained at -68kV. The voltage swing needed to modulate this beam is 4.5kV, which is quite close to the set limit.

As discussed in section **2.2.2**, we can reduce the ripple factor by increasing the magnetic field confinement. When we scale the peak field up by a factor of 1.5, the ripple factor falls from 1.9 to 1.3. This corresponds to an increase in maximum instantaneous efficiency of only about 2%. However, any such increase in efficiency gained by increasing the magnetic field confinement comes at the cost of increased solenoid current and thus increased upkeep in terms of cooling etc.

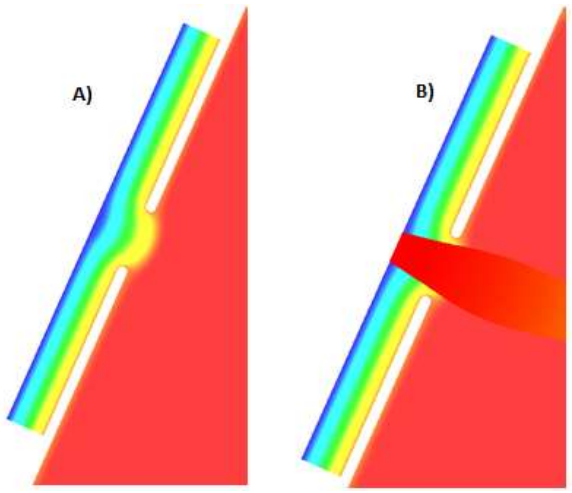

Fig. 26. a) the potential contour plot of the emitter region. The emitter is maintained at -70kV (Blue) and the mod-anode is maintained at -68kV (Red). b) the potential contour plot superimposed with the beam trajectory

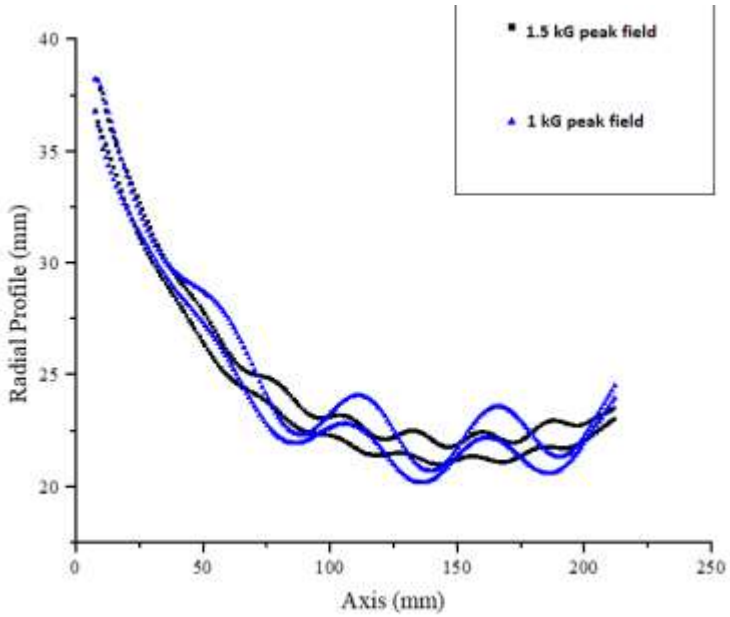

Fig. 27. Radial profile of the beam under different magnetic field confinement. The plot with black square dots represents the radial profile of the electron beam at different axial positions when confined by a magnetic field with peak strength of 0.15 T. The plot with blue triangle dots represents the radial profile of the beam when confined by a magnetic field with peak strength of 0.1 T. The set of lines at top (for both plots) corresponds to the radial profile of electrons at the outermost layer of the electron beam while the set of lines at the bottom corresponds to the electrons at the innermost layer of the beam. The beam width at a given axial position can be found by subtracting the beam radius of the outermost electron and innermost electron

3.2 Effect of electrode geometry

Similar to the discussion presented in section **2.2.3**, the electrode geometry plays an important role in maximizing the device potential. The RF voltage is limited by the fact that we want all beam electrons to reach the collector. Electrons will be reflected if they acquire too much transverse energy on their passage from the cathode through the gap, or if their space charge lowers the potential near the collector by a large amount. The electrode geometry determines the maximum achievable V_{RF} and instantaneous efficiency. Depending on the geometry it is possible to reduce the transverse energy gained by the beam electrons and shield their space charge, and thus maximize the RF voltage.

First we optimized the AK-Gap length while keeping all other parameters fixed. The RF voltage is sensitive to reduction in AK-Gap length since reducing this factor increases the transverse momentum of the beam as a result of the radial component of the electric field from the edges of the mod-anode and anode. Adding transverse momentum to the beam electrons reduces their axial momentum and lowers the potential at which they can be collected. We found the optimum AK-Gap length to be 45 mm. As expected, the ripple factor remains constant as long as the AK-Gap length is greater than 45 mm as shown in Fig. 28.

The same process was carried out while keeping AK-Gap length fixed and changing the anode length. The optimum anode length which reduces the device size while maintaining peak efficiency was found to be 62.5 mm. Any lower than this will significantly affect the device efficiency. This is due to the fact that the decelerating electric field starts influencing the beam current much earlier before it can achieve its maximum kinetic energy via acceleration. As expected, the ripple factor is not affected by change in anode length since the reduction in device

efficiency is due to decreased maximum achievable longitudinal beam energy and not increased transverse beam energy.

The optimal AK-Gap and anode length is thus 45mm and 62.5 mm respectively. Such a device has a maximum RF-voltage (V_{RF}) of 62.75 kV and an instantaneous device efficiency of 89.6%.

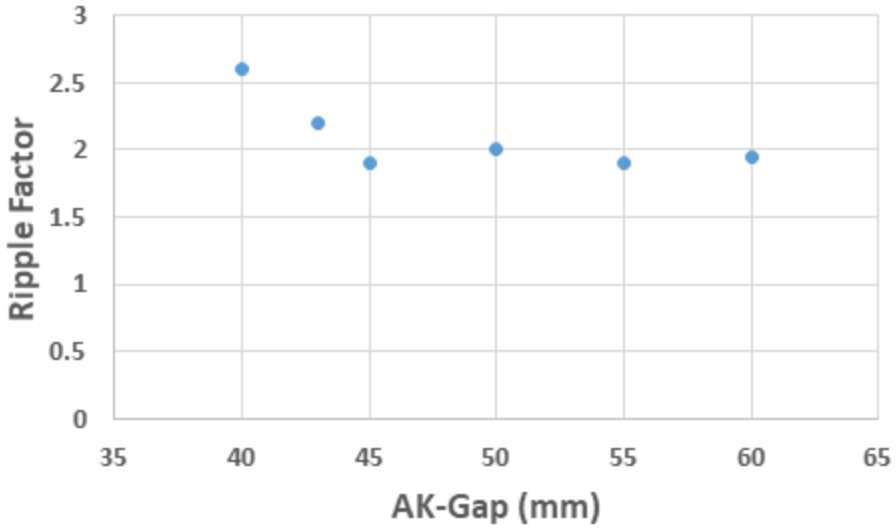

Fig. 28. Ripple factor as a function of AK-Gap length

3.3 Collector design

As mentioned at the beginning of this chapter, as long as the magnetic field confinement was strong, the electron beam closely follows **B** field lines. In the profile shown in Fig. 22 the beam is compressed from a higher radial co-ordinate to a lower value as it approaches the decelerating gap. The curvature of the field line then remains small until it hits the collector of the design. To achieve such a profile, we have simulated a solenoid which is much longer in length than the actual device, with its mid plane being located at the point of the device collector.

It is possible to use much smaller solenoids which will be easier to create and maintain, however we will no longer be able to compress the beam profile.

The field lines form a closed loop, therefore if we use smaller solenoids, then the electron beam will spread out after the decelerating gap. Thus, unlike in the case of Model A we will have to use a bulb shaped collector. Despite the added complexity in such a design there are several advantages in using such a design. One of the major issues which has to be addressed when designing a collector is the problem of heat distribution. It is ideal to have a power density lower than 500 W/ cm^2. This is easily achievable in our case due to the fast rate of expansion of the beam and the larger surface area provided by our bulb shaped collector.

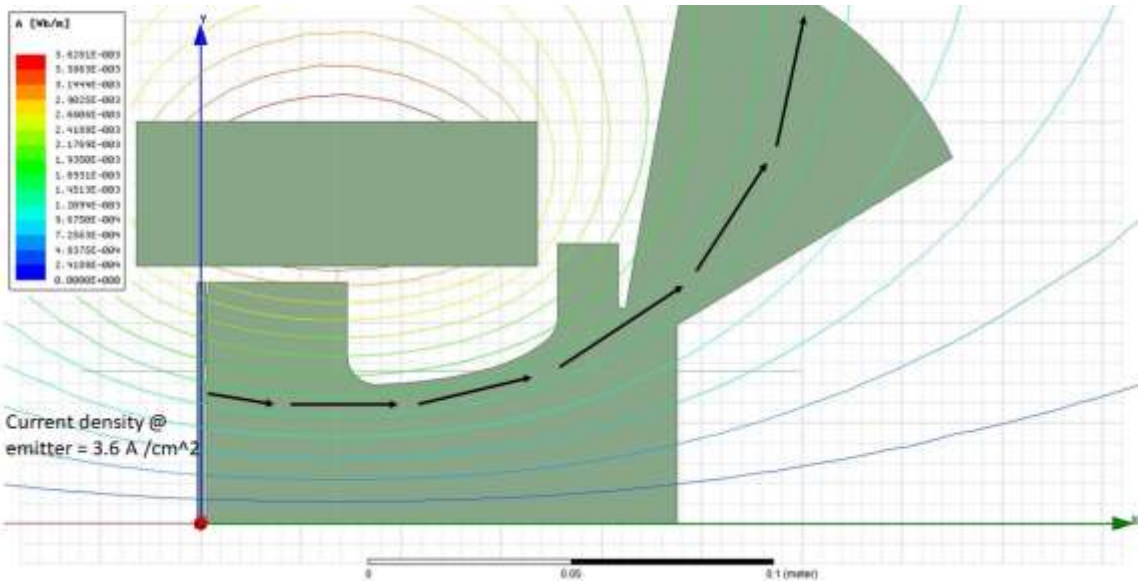

Fig. 29. Magnetic field profile obtained using a simple small solenoid design. The black arrowed lines denote the expected electron beam trajectory

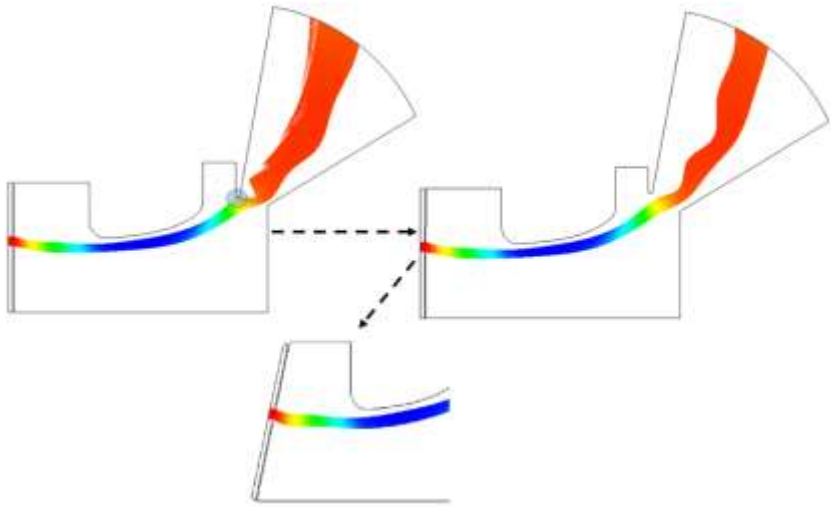

Fig. 30. The steps taken to ensure no interception of the electron beam at the collecting surface

Figure 29 shows the magnetic field profile when using a small solenoid. The black arrowed lines denote the expected beam trajectory. The mid-plane of the solenoid is at the end of the AK-Gap, thus the magnetic field strength decreases as the beam travels from the decelerating gap to the collector. This is advantageous since any secondary electrons produced at the collector that move from collector toward the decelerating gap will face a path of increasing magnetic field and will thus be reflected. This will be discussed in detail in later.

The optimized magnetic field obtained from Maxwell was imported to the Michelle code and we ran a series of static case designs to study the beam trajectory. The device geometry was altered in steps to ensure a smooth laminar flow of the electrons from the emitter to the collector. The emitting plane was to ensure it remained perpendicular to the **B** field lines at the emitter. The anode was shaped carefully so that the electron beam maintains a constant distance to the anode surface. After the optimization of the magnetic field and electrode geometry of the device, we were able to obtain a high instantaneous efficiency of 90%.

3.3.1 Effect of secondary electrons

Unlike the case of Model A, it is necessary for us to take secondary electrons into consideration when designing the collector using static case simulations. This becomes evident when we run the Michelle code for the same model with and without secondary electrons. The maximum RF voltage falls from -63kV to -59kV when we include secondary electrons for the same model. The reason for this becomes evident once we study the potential plots for the two cases as shown in Fig. 31. Fig. 31(a) shows the case without secondary electron and 30(b) shows the case with secondary electron. In Fig. 31(a), the collector surface is fixed at 63kV, there is a small build up in potential as we move to the center of the collector, with the maximum potential of 64kV at the center. In Fig. 31(b), the collector surface is once again fixed at 63kV, however the buildup in the potential is much larger due to the addition of space charge from secondary electrons.

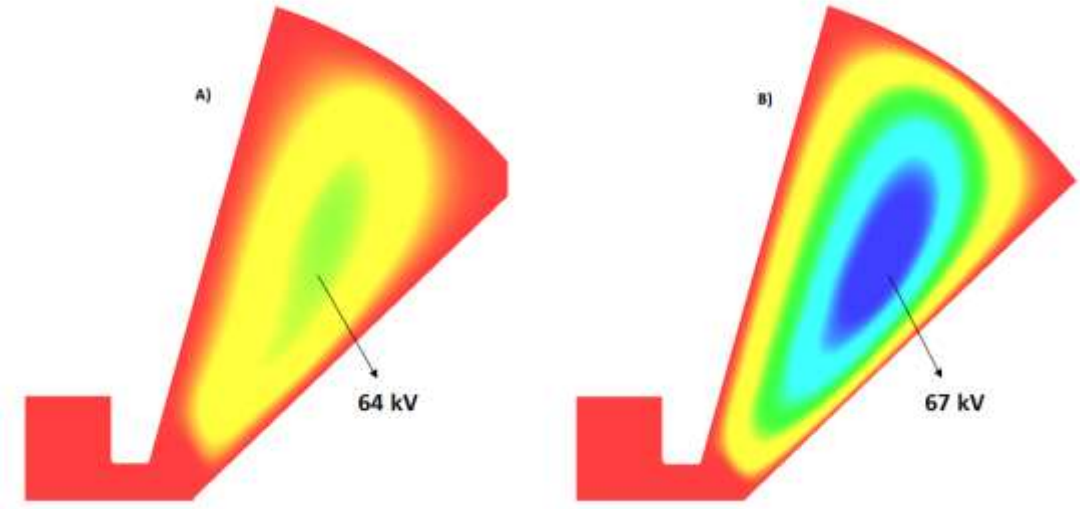

Fig. 31. a) Potential plot without secondary electrons, the collector surface is fixed at 63kV (Red) with the maximum potential of 64kV (Green). b) Potential plot with secondary electrons, the collector surface is fixed at 63kV (Red) with the maximum potential of 67kV (Blue)

The reduction in device efficiency can be easily fixed by enlarging the collector bulb. We were able to obtain an instantaneous device efficiency of about 90% with a much larger collector bulb. This also has an added advantage in the form of much lower power density.

3.4 Time domain simulations

As in the case of Model A in Chapter 2, we next study the device physics by running the optimized model in time-domain mode of the Michelle code. The RF voltage and mod-anode voltage are modulated as shown in Fig. 14. The beam current is switched on at *t = 13 ns* and switched off at *t = 27 ns*.

Unlike the case of Model A, the secondary electrons generated at the collector will have to move along a path of increasing magnetic field as they move from the collector to the decelerating gap. In the case of a static magnetic field (like ours), the dipole moment of the particle μ is conserved. The dipole moment is given by

$$\mu = \frac{0.5\ m\ v_{\perp}^2}{B} \tag{10}$$

where $v_{\perp}$ is the velocity component in the transverse direction and B is the magnetic field. As B increases $v_{\perp}$ increases to maintain μ, thus reflecting the particle back into the collector. The electrons remain trapped in this magnetic mirror as long as they fulfil the trapping condition

$$\frac{v_{\parallel}}{v_{\perp}} \leq \sqrt{\left(\frac{B_{max}}{B_{min}} - 1\right)^2} \tag{11}$$

During the time interval between *t = 13 ns* and *t = 27 ns*, the beam is switched on. The presence of these primary electrons and the magnetic mirror traps most of the secondary

electrons within the collecting surface. As the primary beam intensity reduces in time to zero, the secondary electrons with larger longitudinal velocity escape the confinement and make it to the interaction space consisting of the anode and decelerating gap region. As in the case of Model A, these secondary electrons are accelerated in the negative z-direction until they reach the anode region and encounter the barrier created by the difference in potentials between the mod-anode and anode. These electrons are now trapped between two potential barriers and move back and forth in the interaction space.

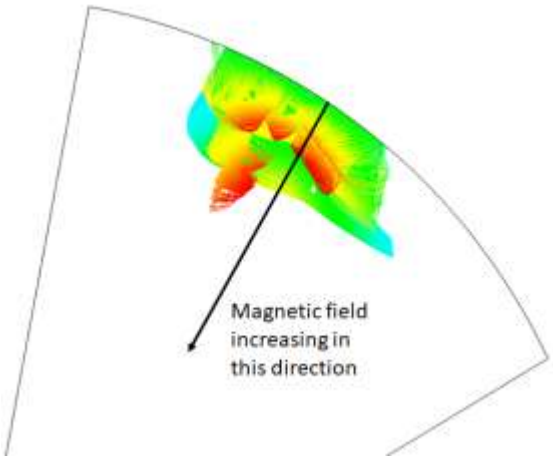

Fig. 32. A snapshot of Michelle time domain simulation showing the secondary electrons trapped within the collector at t = 15ns

Compared with Model A, most of the secondary electrons remain trapped in the collector due to the magnetic mirror as shown in Fig. 33. The loss of efficiency due to interception at anode is quite low and can be easily rectified by increasing the gap between anode and the primary beam. As in the case of Model A, efficiency loss due to interception at anode can also be reduced or completely negated by increasing the strength of the confining magnetic field.

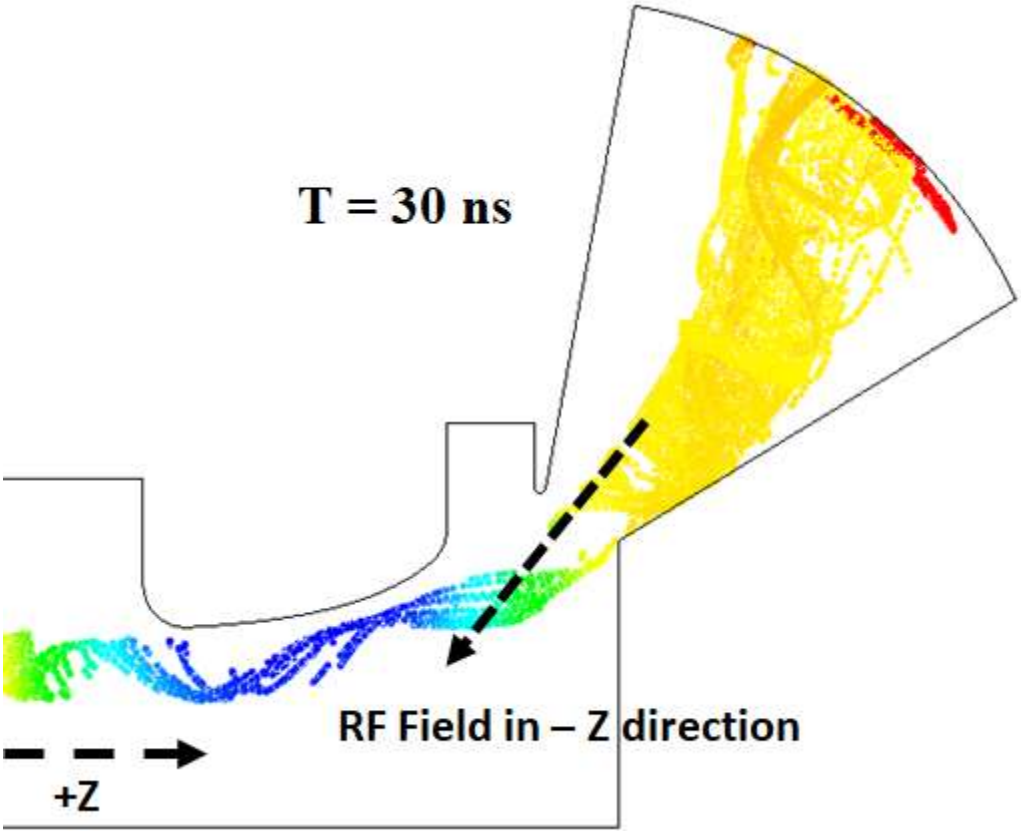

Fig. 33. Snapshot of secondary electron trajectories at t = 30 ns. Most of the secondary electrons are trapped within the magnetic mirror, however those electrons which managed to make it closer to the decelerating gap are pulled into the interaction space consisting of the anode and decelerating gap

3.5 Summary

In Chapter 2 we studied a design employing a uniform magnetic field with no change in beam radius, we studied this simplest configuration with idealized confining magnetic field and maximized the theoretically achievable efficiency. Subsequently, in this chapter we increased the complexity of the problem and explored the steps needed in designing a device with non-uniform magnetic field. As expected the device efficiency reduced when we switched from Model A to Model B. However unlike in Model A, the loss of efficiency due to interception of secondary electrons at the anode is quite low since the majority of the secondary electrons are trapped in the collector due to the magnetic mirror. We were able to optimize the device efficiency by studying

different effects such as electrode geometry, magnetic field profiling and interaction of secondary electrons to obtain a relatively high instantaneous efficiency of 90% and average efficiency of 87.7%. In the next chapter we shall study the third and final model type (Model C) where there is no magnetic field confinement. One of the main advantage of such a device is the compactness of the device since there will be no solenoid. Subsequently, we can also expect the device efficiency of Model C to be lower than Model B since there is no magnetic field to stop the increase in transverse moment of the electron beam.

Chapter 4: Model C – No confining magnetic field

In Chapter 2, we explored Model A which has a constant uniform confining magnetic field. Since we assumed an idealized case for Model A, we were able to obtain a smooth annular beam with constant beam radius. As mentioned in the previous chapter, the downside of such a model would be the large size of the solenoid used to produce the uniform magnetic field. The design discussed in the previous chapter (Model B) is a step in the direction to reduce the size of the gun (Solenoid included). The trade-off is in the form of reduced device efficiency since the non-uniform beam trajectory with changing beam radius leads to increasing energy in the transverse direction as it approaches the decelerating gap. The next step is to explore a device which has no confining magnetic field.

The electron beam emitted from the emitter start expanding due to space charge repulsion as it travels further along the AK-Gap towards the anode. The further the beam propagates, the larger the increase in transverse energy of the beam and device efficiency. Thus, to achieve maximum possible efficiency, the device will have to be quite compact so that beam gains the minimum amount of energy in the transverse direction by the time it reaches the decelerating gap. Thus, compared with the previous two designs, this model will be much more compact. There is also an important added advantage of not requiring a solenoid for magnetic field confinement.

4.1 Designing the device

The placement and angle of inclination of the emitter is quite important as it influences several factors such as device length, beam profile at the interaction region (the region below the anode) and device efficiency. We use Pierce method [21] to calculate the tilt of the emitting

plane required so that the beam clears the decelerating gap without interception. It is important to keep in mind that the CAD design shown in Fig. 34 is cylindrically symmetric with respect to the device axis. For this preliminary iteration of the device, the emitting plane was tilted at an angle of 78.4 degrees with respect to the device axis. The AK-Gap length is fixed at 30 mm and anode length is fixed at 55 mm. We shall be optimizing the electrode geometry (just as in the previous two models) later in the coming section.

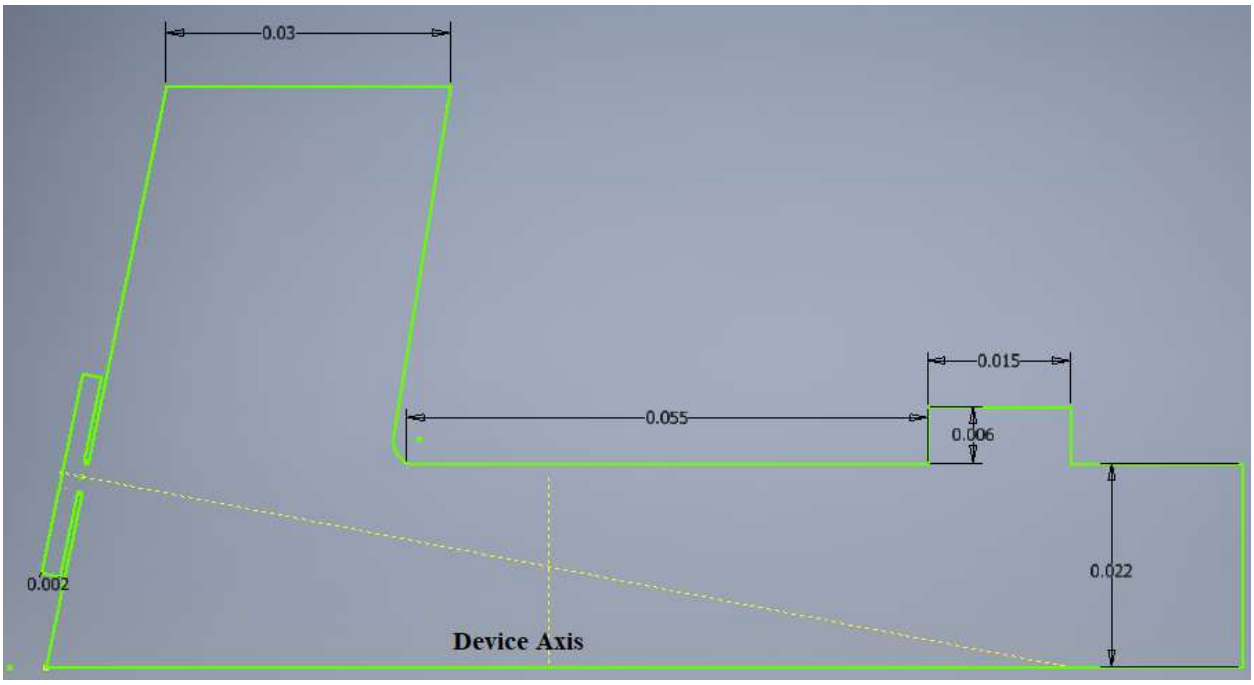

Fig. 34. The CAD design of the design with no magnetic field confinement. The design is cylindrically symmetric. The anode radius is constant in this design. It is possible to mitigate the space charge effects by maintaining a constant clearance between the beam and the anode wall as shown in Fig. 45 **Note:** All units shown in the figure are in meters

The particle trajectories are then simulated using static-case Michelle code. For this initial run, we do not apply any decelerating voltage across the decelerating gap. The emitter is maintained at -70kV and the mod-anode is maintained at -68kV to produce a 30 A beam current. As shown in Fig. 35, the electron beam starts defocusing and expanding right after it is emitted at

the emitter. One of the primary factors which lead to this defocusing effect is the difference in the electric field strength between the two regions. The electric field in the region between emitter and mod-anode is much higher than the electric field in the region between mod-anode and anode. The electron beam passing through the aperture in the mod-anode sees a defocusing effect due to the sudden change in voltage gradient. This defocusing effect can be approximated as a concave lens placed at the aperture and theory behind this effect will be discussed in detail in a later section.

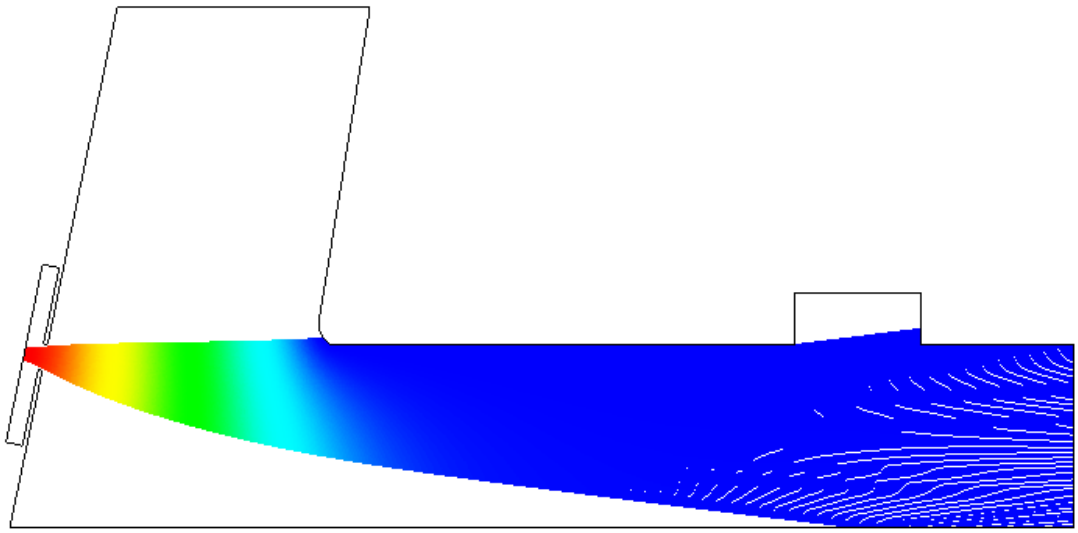

Fig. 35. The electron beam trajectories for the preliminary design. The Emitter is maintained at -70kV and mod-anode is maintained at -68kV to produce a 30 A beam current

The defocusing effect can be reduced by decreasing the electric field difference between the two regions. However, this will require reducing the mod-anode voltage which will in turn reduce the beam current. We can however design a device with two mod-anodes (MA) as shown in Fig. 36. The emitter is maintained at -70kV while the first mod-anode surface (MA 1) is maintained at -67kV and the second surface (MA 2) is maintained at -60kV. Thus, the voltage gradient between emitter and MA 1 is lower than the voltage gradient between MA 1 and MA 2.

This produces a focusing effect at the aperture of the first mod-anode. This fact is evident by also looking at the equipotential contour shape shown in Fig. 36 below. Conversely, the defocusing effect due to the gradient difference between the two regions separated by the second aperture (MA1-MA2 and MA2-anode) has reduced since MA 2 is maintained at -60kV. Thus, by carefully manipulating the electrode potentials it is possible to build a combination of focusing and defocusing aperture lens with a net focusing effect. This theoretically will enable us to propagate the electron beam with low spreading until the decelerating gap. Before we run a number of simulations to find the best combination it is beneficial to study the theory behind aperture lenses and beam transfer matrices.

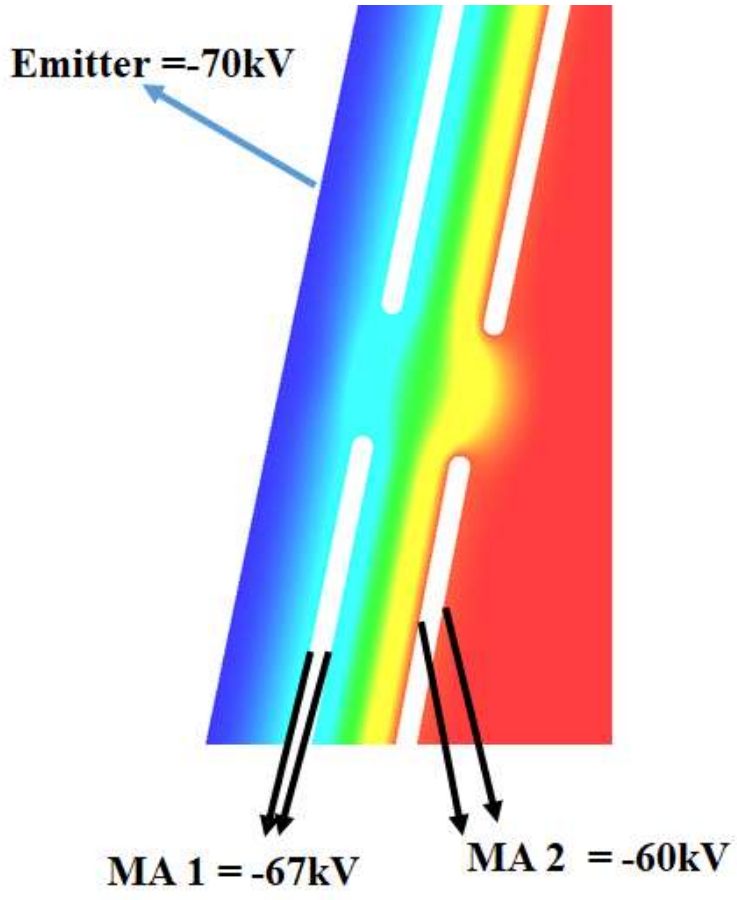

Fig. 36. An enlarged figure of a design with two mod-anodes (MA 1 and MA 2). The emitter is maintained at -70kV (Blue) while MA 1 is at -67kV (Cyan) and MA 2 is at -60kV (Red)

4.1.1 Beam transfer matrices

For the sake of simplicity, we shall be tracing the path of a single electron originating at mid-point of the emitter. The path of this electron can be described using ray optics. Originally, this concept was developed to calculate the propagation of light rays. The ray (which denotes the path taken by our single electron) can be denoted with its transverse offset (r) and its angle of inclination with respect to the reference axis (θ). Assuming the angles involved are small (paraxial approximation), there is a relation between r and θ co-ordinates before and after an optical element.

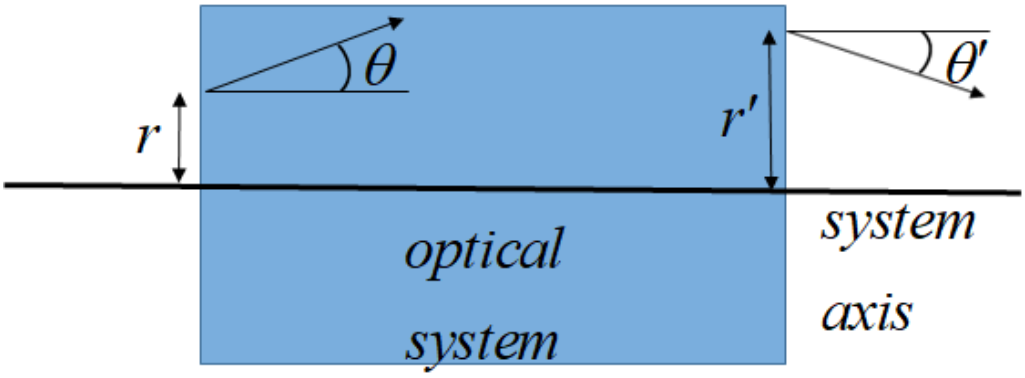

Fig. 37. Figure showing the r and of a ray before and after it passes through an optical system

The optical system is characterized by its ability to modify the co-ordinates of the original ray from (r,θ) to (r',θ'). In the paraxial approximation, when all angles are small so that $\sin(\theta) \approx \theta$, the relation between (r,θ) and r',θ' can be given by

$$\begin{pmatrix} r' \\ \theta' \end{pmatrix} = \begin{pmatrix} A & B \\ C & D \end{pmatrix} \begin{pmatrix} r \\ \theta \end{pmatrix} \tag{12}$$

The 2x2 matrix characterizes the optical element completely since it transforms the original ray depicted by (r,θ) to the final ray given by (r',θ'). Let us now look at the transfer matrix for a simple thin lens with a focal length of *f*. The transverse position remains the same while the angle changes as given by Eq. (19)

$$r' = 1(r) + 0(\theta) \tag{13}$$

$$\theta' = -\frac{1}{f}(r) + 1(\theta) \tag{14}$$

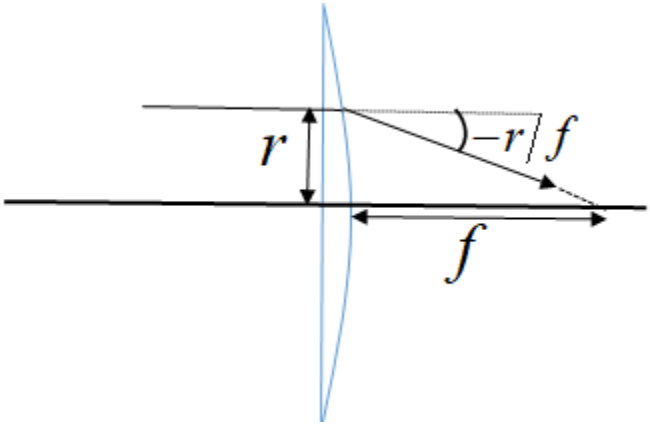

Fig. 38. Effect of a thin lens with focal length f on a particle initially parallel to the axis

Thus the thin lens can be depicted by the matrix **M** given by

$$M = \begin{pmatrix} 1 & 0 \\ -\frac{1}{f} & 1 \end{pmatrix} \tag{15}$$

The matrix for a diverging lens is similar but the sign of the term a_{21} changes to $+\frac{1}{f}$. In general the sign of the term a_{21} of a transfer matrix shows if the element or combination of element is focusing or defocusing the particle.

Similarly we can also calculate the transfer matrix associated with translation in free space along the longitudinal axis (z axis) as shown in Fig. 39. The angle remains unchanged, however the transverse position changes given by

$$r' = 1(r) + d(\theta) \tag{16}$$

Thus the transfer matrix is given by

$$M = \begin{pmatrix} 1 & d \\ 0 & 1 \end{pmatrix} \tag{17}$$

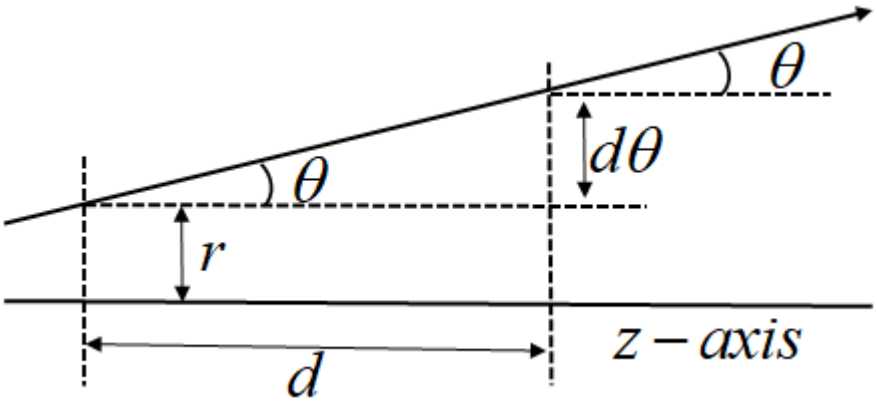

Fig. 39. Modification of a particle trajectory during free space translation

Now that we have defined the transfer matrix for the two elements of interest. It is possible to calculate the co-ordinates of a particle passing through multiple such elements by multiplying (r, θ) with various subsequent matrix elements. Note that the order of matrix multiplication is important. The matrix of the system that is crossed by the ray first is placed to the right, so that it operates on the column matrix of the incident ray or particle.

We shall now look at the theory behind electrostatic focusing or defocusing of a charged particle as it passes through an aperture with varying electric field. The aim is to approximate this effect as a single thin lens which can then be converted into a transfer matrix.

4.1.2 Electrostatic aperture lens

The electrostatic aperture lens is a hole centered axially in an electrode separating two regions with different electric field as shown in Fig. 40.

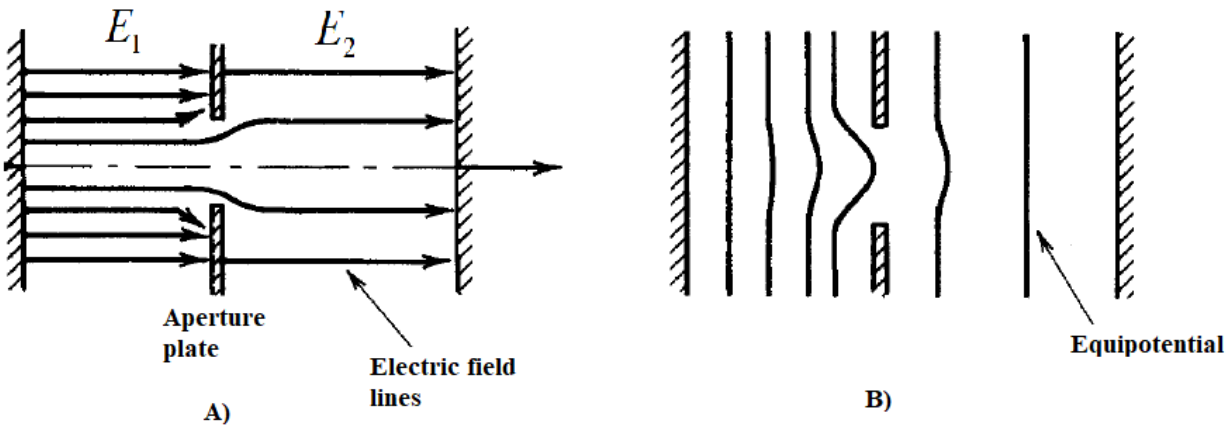

Fig. 40. Figure showing an electrostatic aperture lens. (a) Geometry showing the electric field lines. (b) Equipotential lines. The figure was taken from Theory and Design of Charged Particle beams by Martin Reiser (Pg.81)

Electric fields E_1 and E_2 are produced by applying a voltage relative to the voltage applied on the aperture plate. If the upstream and downstream electric fields vary, there will be radial components of the electric field near the aperture which will produce a focusing or defocusing effect. In the above figure, the axial electric fields are positive on both sides of the aperture plate. The field to the left of the plate is stronger than the field to the right. In this case, the radial fields point outwards as we move from left to right of the aperture. Thus a positively

charged particle will be defocused or in other words the aperture behaves like a concave thin lens. If the field direction is reversed (while keeping the same relative strength) or if the field on the right is stronger (while keeping same field direction), the aperture behaves like a convex thin lens (focusing effect). The amount of transverse impulse on a particle passing through the aperture is directly proportional to the amount of time spent in the radial electric fields. The amount of time spent is inversely proportional to the axial velocity of the particle, which in turn is determined by the axial electric fields. Furthermore, the final axial velocity of the particle depends on the particle direction. These factors contribute to the fact that the focal length of the aperture lens depends on direction of propagation or in other words the focal length of the lens if we pass from left to right will not be same as when we pass from right to left.

The radial electric fields are localized at the aperture. The focal length of the aperture lens can be calculated by making two assumptions:

1) The relative change in radial position as it passes through the aperture is negligible similar to the thin lens approximation.
2) The relative change in axial velocity is negligible as it passes through the aperture.

Consider a particle moving in the +z direction with zero radial velocity ($v_r = 0$). The change in v_r for non-relativistic motion is given by

$$\frac{dv_r}{dz} = \frac{qE_r}{m_o v_z} \tag{18}$$

However we can replace E_r by substituting into Eq. (23) with

$$E_r = -\frac{r}{2}\frac{\partial E_z(0,z)}{\partial z} \tag{19}$$

Thus giving,

$$\frac{dv_r}{dz} = \frac{qE_r}{m_o v_z} \cong -\frac{q}{2m_o v_z} r \frac{dE_z(0,z)}{dz} \tag{20}$$

Following the two assumptions of constant r and v_z in the region of aperture, Eq. (25) can be directly to yield

$$\frac{v_r'}{v_z'} = -qr \frac{E_{z2} - E_{z1}}{2m_o v_{za} v_z'} \tag{21}$$

Where v_z' is final axial velocity of the particle after it passes through the aperture, v_{za} is the particle velocity at the aperture and v_r' is the radial velocity after exiting. The focal length is then given by

$$f \cong r(\frac{v_z'}{v_r'}) \tag{22}$$

Substituting Eq. (26) into Eq. (27) we get

$$f \cong 2m_o v_{za} v_z' / q(E_{z2} - E_{z1}) \tag{23}$$

When the particle kinetic energy is large compared to the energy change passing through the lens ($v_{za} \approx v_z'$), Eq. (28) can be written as

$$f = 4T / q(E_{z2} - E_{z1}) \tag{24}$$

Where T is the kinetic energy of the particle at the aperture.

4.1.3 Designing the device with multiple mod-anodes

We have now introduced the theory behind transfer matrices and aperture lenses, thus giving us the tools required to start designing a device with multiple mod-anodes. First, let us verify the focal length formula shown in Eq. (29) by comparing it with Michelle static-case simulation. We use the preliminary device as shown in Fig. 34 to run the code. The emitter is maintained at -70kV and the mod-anode at -68kV, with a separation of 2 mm between the two electrodes. The anode is maintained at ground and is separated from the mod-anode at a distance of 30 mm. For the sake of simplicity the co-ordinate axis is placed at the center of the emitter and is tilted in such a way that the radial axis is parallel and the longitudinal axis is perpendicular to the emitting plane as shown in Fig. 41.

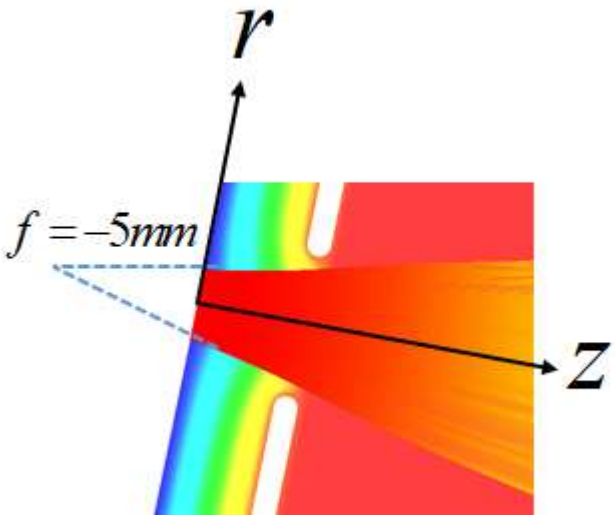

Fig. 41. An enlarged image of the particle trajectories near the emitting region for the device shown in Fig. 34. The focal length of the defocusing lens was found to be -5 mm from the emitter along the Z axis

The focal length of the defocusing lens was found to be roughly 5 mm behind the emitter. The kinetic energy of an electron as it is accelerated from rest from a potential of -70kV to a potential close to -68.25kV can be easily calculated. Since we tilted the co-ordinate system, it is

quite simple to find E_{z2} and E_{z1} ($E_{z2} \cong -2.275 \frac{kV}{mm}$ and $E_{z1} = -1 \frac{kV}{mm}$). Thus substituting T, E_{z1} and E_{z2} into Eq. (29), we obtain a focal length of -7.1 mm. Thus the value which we obtained theoretically is in close agreement with the simulation result. The deviation can be explained due to the fact that the electrons experience the defocusing effect right after they are emitted from the emitter, while in the theory, the effect is experienced at the aperture in the form of a thin lens. The distance between the emitter and the thin lens is approximately 2.5 mm, thus taking this into factor the focal length of -7.1 mm is within the degree of expected error.

We now proceed to the design with two mod-anodes as shown in Fig. 36. Since the focal length of the aperture lens is determined by the relative strength of the electric field, we shall keep the geometry of the two mod-anode sections the same. The aperture lens formed by these two mod-anode apertures are separated by a distance of 3 mm, thus forming a cascade of electrostatic components as shown in the Fig. 42.

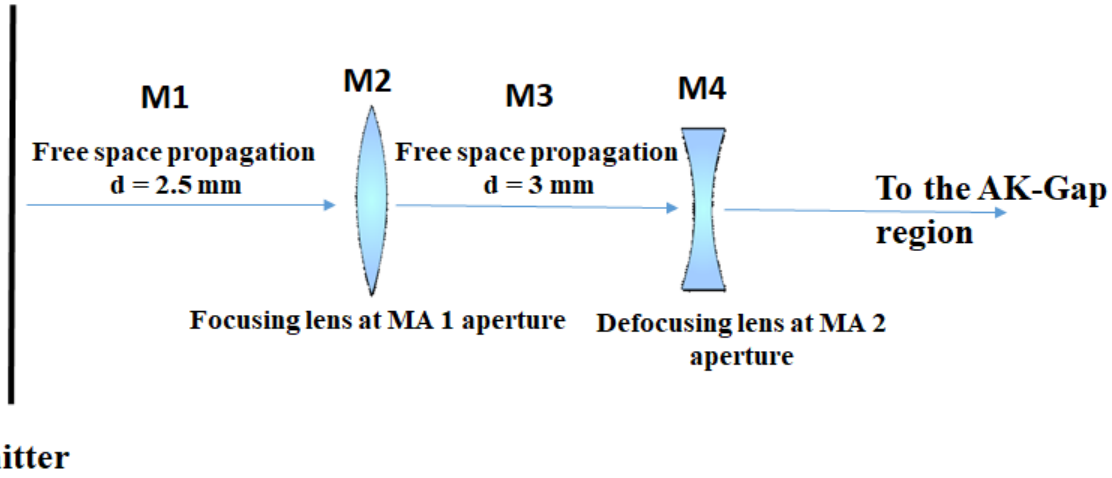

Fig. 42. A schematic showing the cascade of various components involved in the calculation of the effective transfer matrix for the design with two mod-anodes

The effective transfer matrix that computes the particle co-ordinates after the second mod-anode aperture is given by

$$M_{eff} = M_4 M_3 M_2 M_1 \tag{25}$$

Where M_1 and M_3 is the transfer matrix for free space propagation as given by Eq. (22). M_2 and M_4 is the transfer matrix for the aperture lens at MA 1 and MA 2 respectively, they can be calculated by using Eq. (20). As always, the emitter is fixed at -70kV, while the first mod-anode is fixed at -68kV. The a_{21} term of M_{eff} must be zero since we want the beam to stay collimated once it exits the second mod-anode. Using this condition we can calculate the potential of the second mod-anode. According to our calculations, the second mod-anode has to be maintained at a potential of -58kV to perfectly collimate the beam.

A static-case simulation was performed for the design with two mod-anodes. We fix the various electrode surfaces as required by our theoretical predictions. Figure 43 shows the electron trajectories simulated by the Michelle code. The beam is better confined when compared with our initial design shown in Fig. 35, however, the beam is still not perfectly collimated. The beam width right after the second mod-anode is the same as when it is emitted at the emitting plane and remains roughly the same for a short period. This follows our theoretical prediction, however as the beam travels further into the AK-Gap region it begins expanding due to space charge repulsion. The electric field between the two mod-anodes is roughly 5 kV/mm and is quite high. Any further increase in the field will be risky since we are already operating close to the electrical breakdown of vacuum. Thus it is more feasible to operate the device at present parameters while optimizing AK-Gap length, anode length and geometry.

It is also possible to obtain a better confinement by using more mod-anodes so as to increase the number of focusing aperture lenses and reducing the strength of the final defocusing

aperture lens at the final mod-anode aperture. Figure 44 shows the particle trajectories of a design with 4 mod-anodes. The electron beam is much better confined as compared with that shown in Fig. 43. However, one of the main downside of using multiple mod-anodes is the increase in complexity in terms of the switching components involved in modulating the voltage of these mod-anodes.

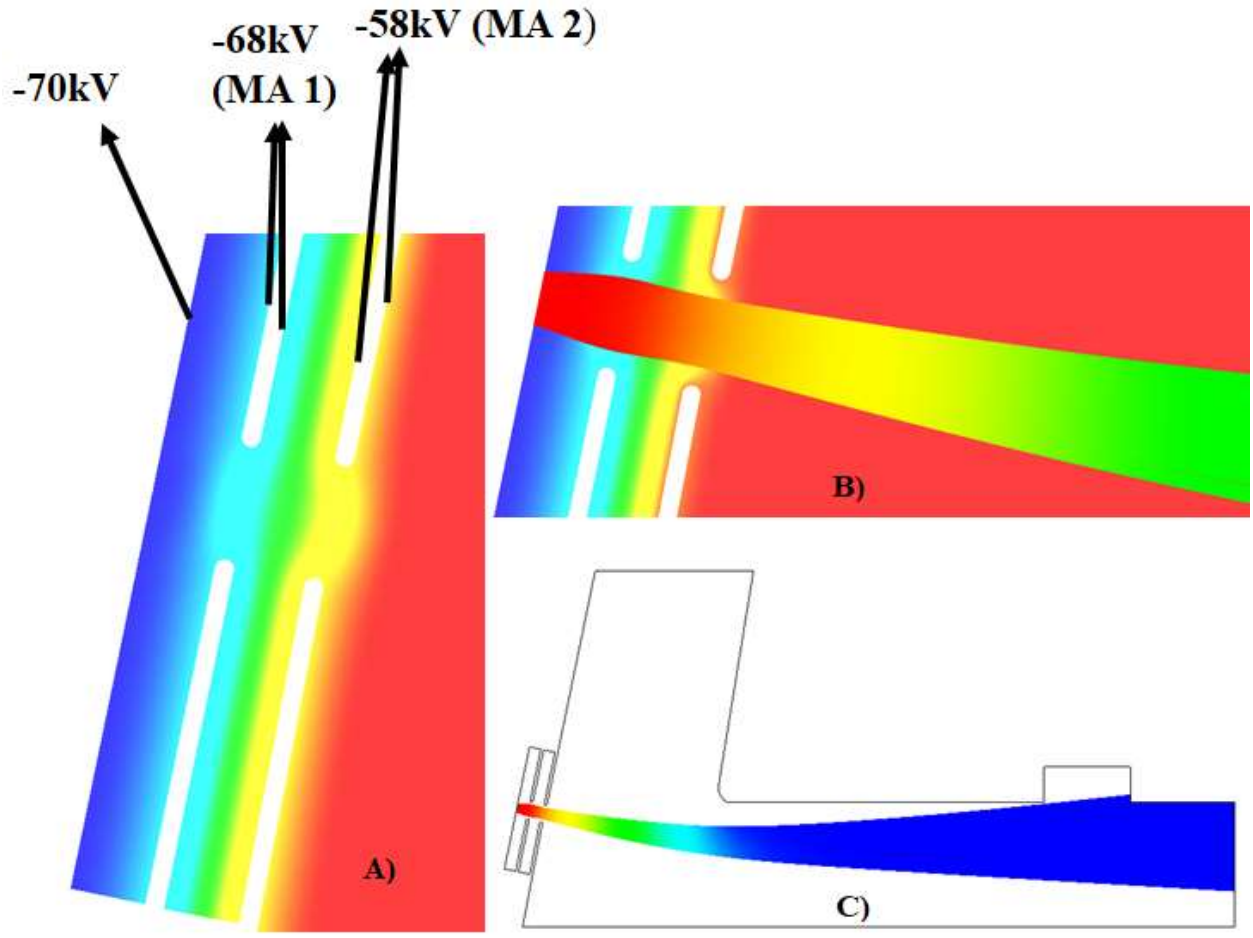

Fig. 43. The simulation result for the design with two mod-anodes. a) An enlarged image of the emitter and mod-anode region. b) An enlarged image showing the collimation of the beam due to the combination of the two mod-anodes. c) The particle trajectories

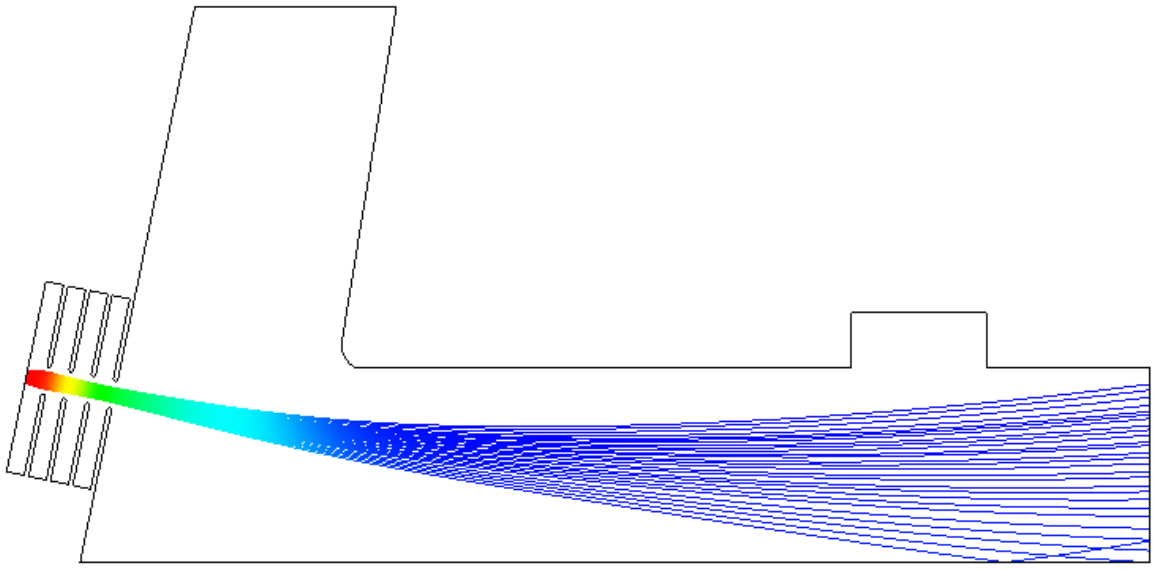

Fig. 44. The particle trajectories of the design with 4 mod-anodes

4.1.4 Optimizing AK-Gap length, Anode length and geometry

Using the results obtained from the previous section, we fix the MA1 potential at -68kV and MA2 potential at -58kV. A decelerating RF voltage ($-V_{RF}$) is applied across the decelerating gap. Just as in the case of Models A and B, we find the maximum allowed RF voltage ($V_{RF,\max}$). While keeping the anode length fixed, the AK-Gap length is reduced until $V_{RF,\max}$ reduces. The RF voltage remains fixed until the AK-Gap length falls below 26.5 mm. Once the AK-Gap length is optimized, the anode length is reduced while keeping rest of the parameters fixed. The optimal anode length which minimizes the device size while maintaining $V_{RF,\max}$ was found to be 34 mm and reducing the anode length any further will decrease the device efficiency. The maximum RF voltage is much more sensitive to anode length changes compared with the other two models since Model C is much more compact. Further decreasing the anode length will significantly affect the device efficiency. This is due to the fact that the decelerating electric field

starts influencing the beam current much earlier before it can achieve its maximum kinetic energy via acceleration.

The anode and decelerating gap was reshaped in such a way to maintain a constant clearance between the top layer of the electron beam and the electrode surfaces as shown in Fig. 45.

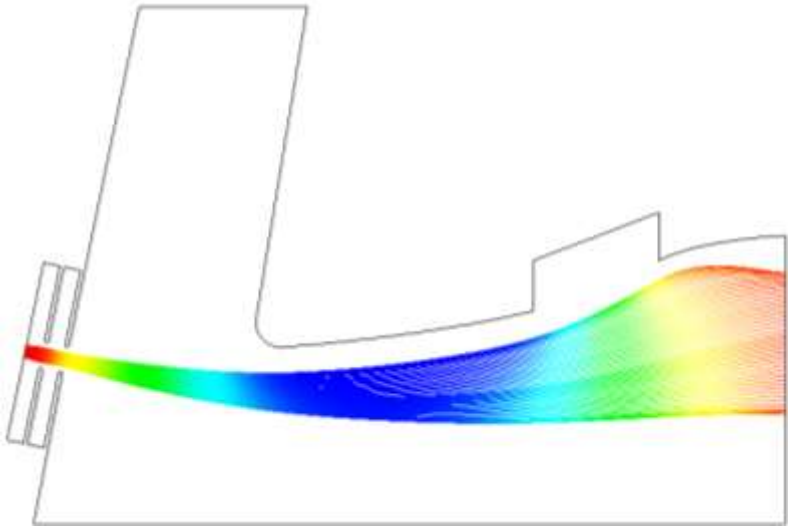

Fig. 45. Model C with two mod-anodes and optimized AK-Gap length, anode length and geometry

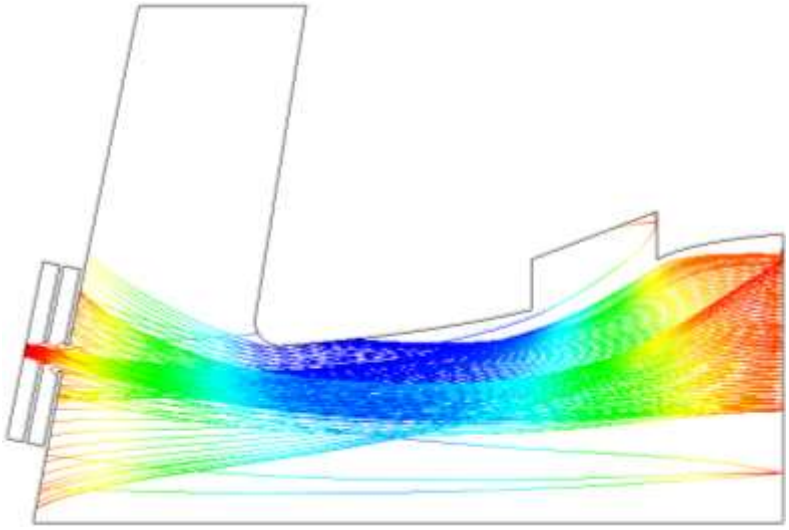

Fig. 46. The particle trajectories of the optimized Model C with primary and secondary electrons included

$V_{RF,\max}$ for the above optimized device was found to be 62.3kV, thus giving an instantaneous maximum efficiency of 89%. It is important to note that secondary electrons were not considered for this simulation. Once the secondary electrons are included into the picture, the device efficiency falls down by a large factor since we are using a flat perpendicular collector, which is quite close to the decelerating gap. The secondary electrons generated at the collecting surface are accelerated back into the interaction region due to the influence of the RF voltage as shown in Fig. 46.

4.1.5 Collector design

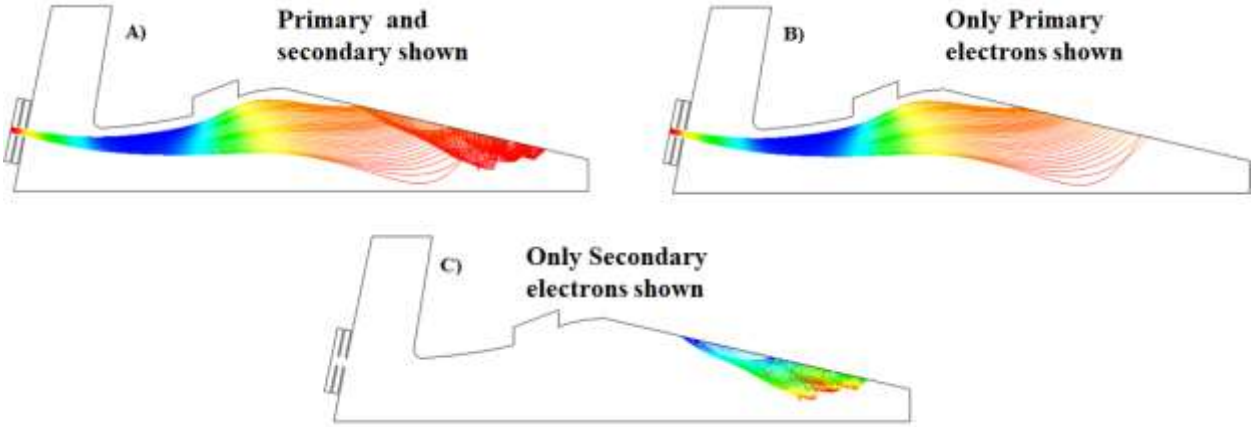

Fig. 47. Model C with slanted collector. a) Primary and secondary electron trajectories shown. b) Only primary electron trajectories shown. c) Only secondary electron trajectories shown

It is necessary to design the collector in such a way to prevent the backflow of the secondary electrons as shown in Fig. 46. We have to ensure that the primary electrons strike the collector far away from the influence of the electric field caused by the RF voltage across the decelerating gap. We employ the slanted collector design used earlier in Model A. Such a design has an added advantage in terms of larger area of collection, thus reducing the average power density at the collector below the threshold of $500 W / cm^2$. In this particular case, we estimate

the average power density to be $410\,W/cm^2$. This is slightly lower than in the case of Model A ($450\,W/cm^2$). With the reduction in device efficiency (compared with Model A) we would expect to see an increase in the beam density deposition on the collector. However, the area of deposition, in this case, has increased by a factor of 2, giving a reduced beam density deposition at the collector.

Figure 47(a) shows the primary and secondary electron trajectories in Model C with slanted collector. The secondary electrons are confined well within the collector space and far away from the influence of the accelerating field across the decelerating gap. The primary electrons repels the secondary electrons back into the slanted collecting surface, where they skip down the surface as shown in Fig. 47(c).

It is important to note that the particle trajectories shown in Fig. 47 were obtained using static-case simulation results, where the primary beam is always present. It is highly likely that the secondary electrons produced at the collecting surface will escape from the collecting region once the primary beam is switched off. It is therefore important to study the secondary electron dynamics during the whole RF cycle using time-domain simulations.

4.2 Time-Domain simulations

We next study the device physics by running the optimized model with slanted collector in time-domain mode of the Michelle code. The RF voltage and beam current are modulated as shown in Fig. 14. To switch the device on and generate a beam current of 30 A from the emitter, MA1 has to be switched from the cut-off voltage potential of -74kV to -68kV, while MA2 needs

to be switched from -74kV to -58kV. The beam current is switched on at *t = 13 ns* and switched off at *t = 27 ns*.

Figure 48 shows the particle trajectories right after the primary electron beam is switched on at *t = 16 ns* and right before the primary beam is switched off at *t = 24 ns.* As can be seen by looking at Fig. 48(b), the secondary electrons are forced to remain within the collecting region due to the influence of the primary electrons. However, once the primary beam current starts reducing, the secondary electrons which were previously trapped start escaping from the collecting region as shown in Fig. 48(c) and Fig. 48(d). Once these secondary electrons near the decelerating gap, they are reaccelerated back into the interaction space below the anode surface. Unlike in Model A (see Fig. 20), the potential barrier formed due to the voltage difference between the second mod-anode and anode is not strong enough to fully reflect these secondary electrons back in the +z direction.

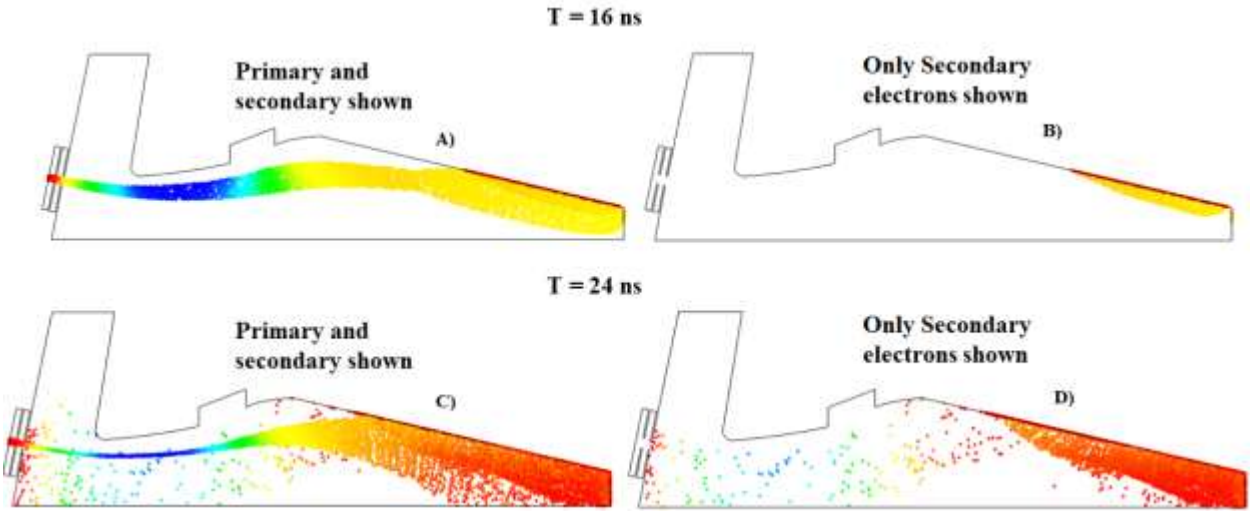

Fig. 48. Particle trajectories at t = 16 ns and t = 24 ns. a) Primary and secondary electron trajectories at t = 16 ns. b) Secondary electron trajectories at t = 16 ns. c) Primary and secondary electron trajectories at t = 24 ns. d) Secondary electron trajectories at t = 24 ns

The secondary electron dynamics once the primary beam is switched off $t = 27\ ns$ has many similarities to its Model A counterpart as discussed in Chapter 2. The secondary electrons which escape the collecting region are trapped within two potential barriers and they travel back and forth between these two barriers. Due to the lack of any magnetic field confinement, these electrons are much more spread out unlike in Model A. Thus, some of these electrons are absorbed by the grounded anode until the potential barrier at the decelerating gap falls in strength and the remaining secondary electrons make it back into the collecting region as shown in Fig. 49(a) and Fig. 49(b).

After $t = 40\ ns$, the RF field reverses polarity (see Fig. 15). Thus, the secondary electrons are no longer accelerated in the –z direction from the collecting region. As the RF field across the decelerating gap gains strength, those secondary electron closer to the decelerating gap are pushed towards the +z direction as shown in Fig. 49(c-f).

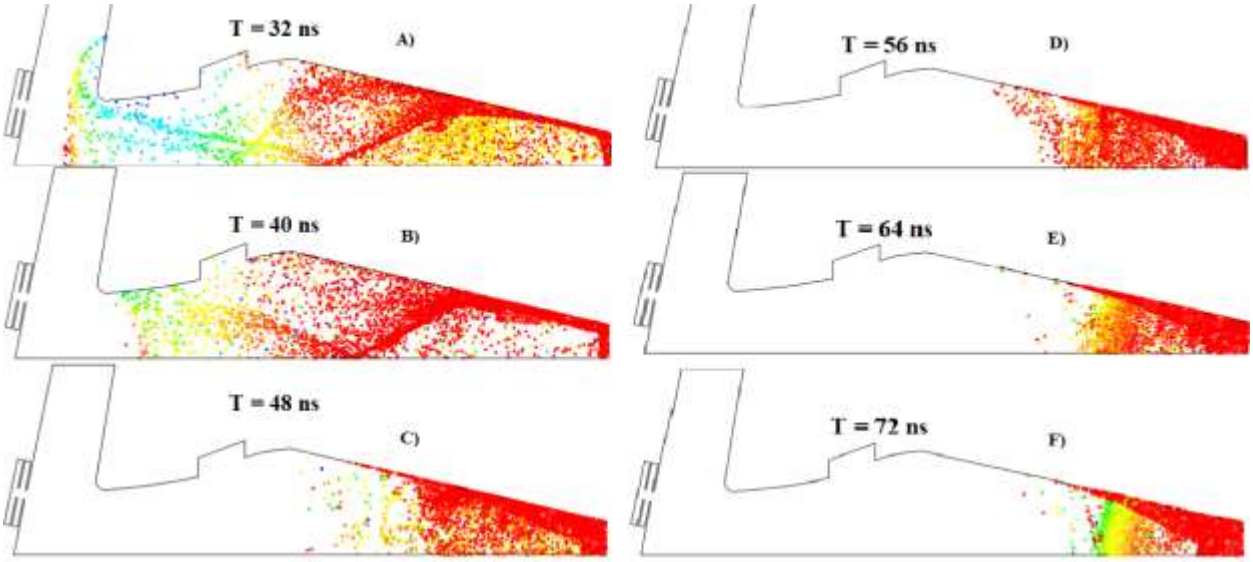

Fig. 49. a) The secondary electron trajectories at t = 32 ns. b) The secondary electron trajectories at t = 40 ns. c) The secondary electron trajectories at t = 48 ns. d) The secondary electron trajectories at t = 56 ns. e) The secondary electron trajectories at t = 64 ns. f) The secondary electron trajectories at t = 74 ns

Unlike in the case of Model A or B, where the secondary electrons were all reabsorbed and removed from the simulation by the end of RF cycle at $t = 80\ ns$, the clump of secondary electrons shown in Fig. 49(f) remains until the simulation ends at $t = 80\ ns$. It is therefore necessary to run a simulation with at least 2 RF cycles and a duration of *160 ns*.

Fig. 50 shows the particle trajectories at $t = 22\ ns$ and $t = 22 + T\ ns$. Where T is the time period of 1 RF cycle (*80 ns)*. The particle trajectories and dynamics remains practically unchanged.

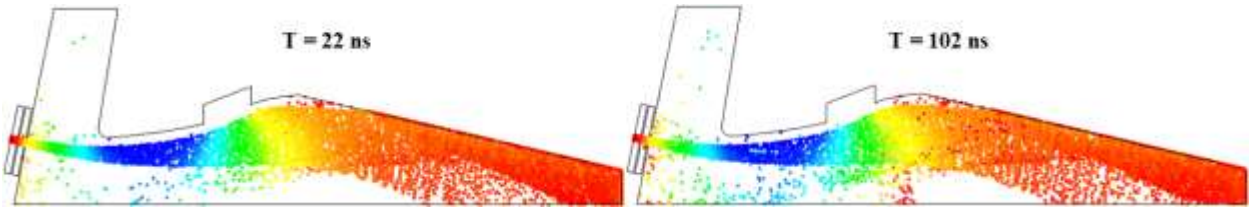

Fig. 50. Particle trajectories at t = 22 ns and t = 22 + T ns

The only visible difference between the two trajectories is the increased particle count due to carryover secondary electrons from the previous cycle. Fig. 51(a) shows the total particle count as a function of time. As expected the curve characteristics of the 2nd cycle is similar to that of the 1st cycle, with an expected offset due to the added number of secondary electrons from the previous cycle.

Despite the increased particle count in the second cycle, the total charge within the device remains roughly the same during the second cycle as shown in Fig. 51(b). The reason for this interesting phenomenon becomes apparent once we study the potential plot at $t = 160\ ns$, as shown in Fig. 52. Despite the large number of secondary electrons aggregated at this region, it causes a negligible potential depression after 2 cycles. The Michelle code assigns varying charge

density for secondary electrons. The secondary electrons left-over at the end of the simulation are those particle types with extremely low charge associated with them. It would be ideal to employ a system to flush the device periodically to remove these aggregated secondary electrons from the collecting region.

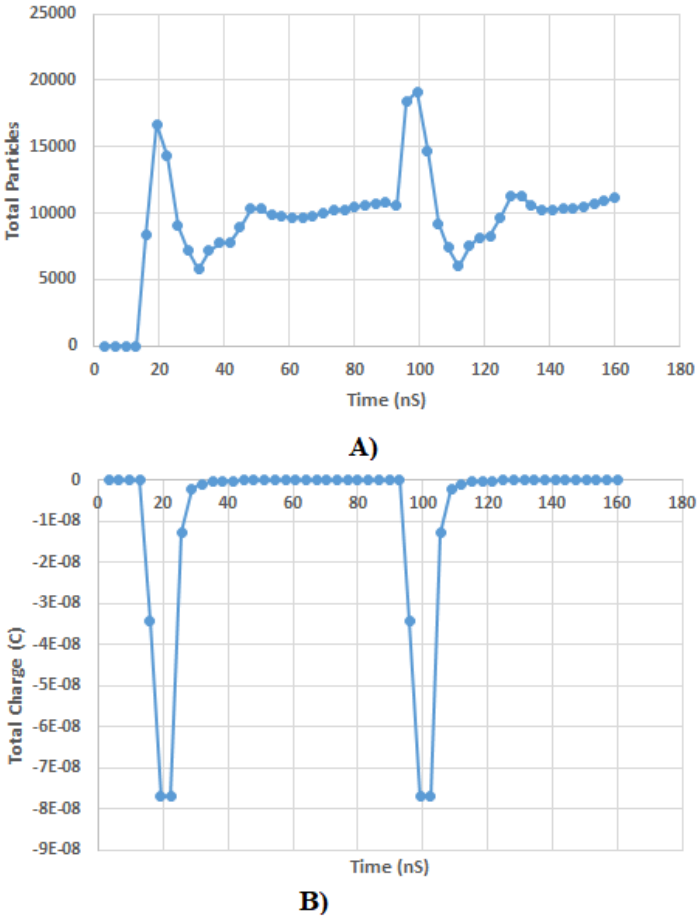

Fig. 51. a) The total particle count within the device as a function of time (ns). b) The total charge (primary and secondary electrons included) within the device as a function of time (ns)

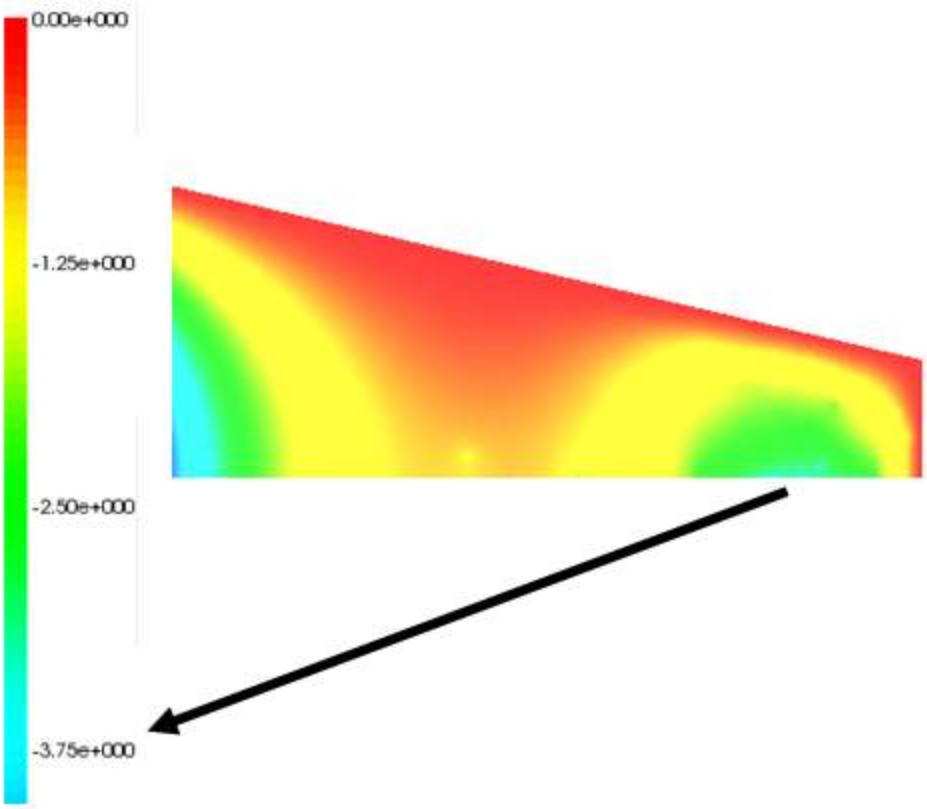

Fig. 52. An enlarged image of the potential plot of the collecting region at t = 160 ns. The collector is maintained at zero potential. The lowest voltage is roughly -3.75 V (caused due to space charge potential depression)

4.3 Summary

The beam confinement was improved by using multiple mod-anodes. We used various theoretical tools such as transfer matrices and electrostatic aperture lens to model and optimize the device with multiple mod-anodes. We studied the secondary electron dynamics using static and time-domain Michelle simulation for the optimized device design. Unlike the previous two models, the secondary electrons are still present at the end of the RF cycle. Michelle time-domain simulation results predicts that the charge associated with these secondary electrons is extremely low and thus they do not affect the device efficiency during the next cycle.

The power contained in the secondary and reflected electrons accounts for roughly about 5.9% of the incoming beam power, the vast majority of which was absorbed by the anode as shown in Fig. 49(a). This is disadvantageous since this reduces the instantaneous device efficiency from roughly 89% to 83.1% and average device efficiency to 81%. While the device efficiency of the Model C type device is the lowest of the three models, it is much more compact compared with Model A and Model B. The additional complexities involved with solenoid upkeep and loss of efficiency due to powering the solenoid system is also absent in this device model.

Chapter 5: Conclusion

Ionospheric heaters broadcast high power radio waves to induce controlled modification of the ionosphere. These heaters have been used to research the ionosphere, upper atmosphere, and plasma turbulence. High-frequency Active Auroral Research Program in Alaska and Sura Ionospheric heating facility in Russia are some examples of fixed ground-based facilities around the world. These fixed ground-based facilities do not have the capability of supporting research at different latitudes. The large size and low efficiency of individual heating units used in these facilities prevent their reuse in mobile structures. These factors motivate the need for developing a novel, highly efficient mobile ionospheric heaters. Ionospheric heaters consist of three major subsystems: RF Power source, Power extraction circuit, and an antenna. This thesis aims at designing one of these subsystems, a highly efficient megawatt-class RF power source.

We propose a novel grid-less version of the tetrode operated in class D mode as the highly efficient megawatt-class RF power source for the mobile heater. Three different device configurations were studied in detail. Model A with constant magnetic field confinement and beam radius profile, Model B with a tapered magnetic field and non-uniform beam radius profile, and finally Model C with no magnetic field and non-uniform beam radius profile.

The instantaneous maximum efficiency and average efficiency given by Eq. (2) and Eq. (3) for the three different models were obtained using Particle-In-Cell Michelle code. Maximizing average efficiency involves a trade-off between pulse duration and peak beam current. The peak instantaneous efficiency depends on the beam current, magnetic field (if present), collector geometry, and interaction between primary and secondary electrons.

The effect of changing the AK-gap length, anode length, and anode geometry on maximum RF voltage and device efficiency was studied for all three models. Reducing the AK-gap increases the radial electric field, which, in turn, increases the transverse energy of the beam current, thus reducing the device efficiency. Similarly, reducing the anode length reduces the maximum energy gained by the primary beam via acceleration. The device efficiency is more susceptible to changes in AK-gap length and anode geometry than the anode length. Thus, it is possible to optimize the device geometry and make it much more compact whilst still operating with high efficiency.

The instantaneous device efficiency is dependent on the space charge potential (V_{SC}) as given by Eq. (6). However, the space charge potential increases due to the inclusion of secondary electrons. The effects of the inclusion of secondary electrons were studied using time-domain simulations. The axial and transverse momentum evolution of beams with and without secondary electrons was studied across different cross-sections to understand the interaction between the primary and secondary beam currents. The secondary electron dynamics in the absence of primaries were also studied.

In the case of all three models, no cathode bombardment was detected due to the presence of the strong repelling field in the AK-gap. In Models A and C, there is a significant efficiency loss due to the absorption of secondary electrons at the grounded anode. However, in the case of Model A, this can be negated by optimizing the device geometry by changing the AK-gap length, anode length & anode geometry. This method is not very effective for Model C since the secondary electrons are largely scattered due to the lack of a guiding magnetic field. The efficiency loss in Model B due to interception at the grounded anode is minimal. This is due to

the fact that the vast majority of the secondary electrons remain trapped within the collector region due to the magnetic mirror.

In short, time-dependent simulations revealed two important issues in the operation of Model A and B: 1) even in the absence of a primary electron beam there is no cathode bombardment by the secondaries; 2) by the end of the positive half period of RF voltage, all secondaries disappear, hence there is no accumulation of electron clouds. In the case of Model C, while there was no cathode bombardment, we see an increase in particle count as the number of RF cycles increases. These aggregated secondary electrons have an extremely low charge associated with them and thus does not affect the device efficiency.

In conclusion, after optimization, Model A has the highest instantaneous and average device efficiency of 93.9% and 91.5% respectively. It is followed by Model B with an instantaneous and average device efficiency of 90% and 87.7% respectively. Finally, Model C has the lowest (Compared with Model A and B) instantaneous and average device efficiency of 83.1% and 81% respectively. The choice of the optimal design for real systems may depend on a number of tradeoffs. In the situations where the weight and size of a system play a crucial role, Model C could be more preferable with the penalty of lower efficiency. In turn, Model A can offer the highest efficiency, but the solenoids required for maintaining a constant magnetic field along the entire device could be very heavy and bulky. In comparison, Model B offers a middle ground among the three models on compactness and efficiency.

For future work, more simulations can be performed to further optimize the three different models. For example, the relationship between collector surface properties and secondary electron emission yield (SEY) is quite interesting. By studying the SEY for different

materials we should be able to further optimize the device efficiency by reducing the number of total secondary electron generation.

References

1. B. Eliasson and K. Papadopoulos, J. Geophysics Research, 121, 3, 2727 (2016).

2. B. L Beaudoin, G. S Nusinovich, G. Milikh, A. Ting, S. Gold, J. Appanam Karakkad, Journal of Electromagnetic Waves and applications 31 (17), 1786-1801

3. HAARP Research and Applications. Committee report convened under the auspices of Air Force Philips Laboratory and the Office of Naval Research auspices, K. Papadopoulos, Chairman; 1995.

4. D. H. Preist and M. B. Schrader, Proc. IEEE, 70, 1318 (1982).

5. A. Zolfghari, P. MacGibbon, and B. North. Proc. EPAC 2004; Lucerne, Switzerland, p. 1093.

6. R. Carter, IEEE Trans. Electron Devices, 57, 720 (2010).

7. M. B. Shrader, D. H. Priest and R. N. Tornoe, Proc. 1993 Particle Accelerator Conference of IEEE, Vol. 2; Washington, DC, p. 1103.

8. N. O'Sullivan and M. Edwards, IEEE-IVEC; Rome; 2009. p. 423.

9. A. V. Galdetskiy, IEEE-IVEC; Rome; 2009. p. 421.

10. E. L. Wright, K. T. Nguyen, J. A. Pasour, S.J. Cooke, B. Levush, J.J. Petillo, I.A. Chernyavskiy, J.F. DeFord, B.L. Held and M. Cusick , IEEE-IVEC; Rome; 2009. p. 117–118.

11. R. L. Ives, M. Read, D. Marsden, G. Collins and R. Karimov, IEEE Int. Conf. Plasma Science; San Francisco, CA; 2013. p. 1.

12. G. Mourier, G. Faillon and P. Garin, Int. J. Electronics, 61, No.6, 715, (1986).

13. R.S. Simon, Technical Digest, IEDM 1986, pp. 156-159.

14. W. D. Kilpatrick, Rev. Sci. Instrum. **28**, 824 (1957).

15. B. Esser, S. R. Beeson, J. C. Dickens, J. J. Mankowski, T. M. Antonsen, Jr., and A. A. Neuber, IEEE Trans. Plasma Sci. **45**(6), 1051–1057 (2017).

16. J. J. Petillo, K. Eppley, D. Panagos, P. Blanchard, E. Nelson, N. Dionne, J. Deford, B. Held, L. Chernyakova, W. Krueger, S. Humphries, T. McClure, A. Mondelli, J. Burdette, M. Cattelino, R. True, K. T. Nguyen, and B. Levush, IEEE Trans. Plasma Sci. **30**(3), 1238 (2002).

17. J. J. Petillo, E. M. Nelson, J. F. Deford, N. J. Dionne, and B. Levush, IEEE Trans. Electron Devices **52**, 742 (2005).

18. J.A. Watson, E.G. Cook, Y.J. Chen, R.M. Anaya, B.S. Lee, J.S. Sullivan, S.A. Hawkins, F.V. Allen, and B.C. Hickman, Particle Accelerator Conference 2001, Chicago, IL, 2001

19. I. D. Smith, PHYSICAL REVIEW SPECIAL TOPICS - ACCELERATORS AND BEAMS, VOLUME 7, 064801 (2004)

20. N. Dionne, “Comprehensive secondary emission modeling for simulating E-beam collection in MICHELLE”, Proc. IEEE Int. Conf. Plasma Sci., 1999

21. “Charged particle beams”, Stanley Humphries, John Wiley and Sons, 1990, Chapter 7